Article

Rainfall characteristics in the central Andes of Peru from a vertically pointed profile rain radar and in-situ field campaign

Shailendra Kumar*, Carlos Del Castro, Jairo M. Valdivia Prado, José Luis Flores Rojas, Stephany M. Callañaupa Gutierrez, Aldo S. Moya Alvarez, Elver Villalobos Puma, Daniel Martinez Castro, Yamina Silva

Corresponding author: Shailendra Kumar
email address: shailendrak89@gmail.com; skumar@igp.gob.pe
Address: * Institute of Geophysics, Lima, Peru Institute of Geophysics, Lima, Peru

Abstract: present study uses the 3 years of data from a vertically pointed profile Radar (VPPR) at the mountain site (Huancayo at 3.2 km msl; HYO) in Peru to investigate the precipitation characteristics/patterns including diurnal variation, bright band (BB) characteristics and vertical structure of rain (VSR). VPPR provides continuous 1-min profiles of radar reflectivity (Z_e), rain rate (RR), liquid water content (LWC) and Doppler velocity. At the same time, field campaign data are used to investigate the role of the surface and atmospheric variables in generating the rainfall and organization of the cloud systems over HYO. The precipitation shows the bimodal distribution; frequent and higher RR during afternoon and nighttime. The BB height also shows a diurnal pattern and BB height is higher during afternoon and nighttime compared; and follows the diurnal heating of the Andes. More than 70% BB height lies between ~4.3-4.7 km and only 20% BB has altitude higher than 5 km. The austral summer monsoon (December to March months) have higher intense vertical profiles (higher Z_e) compared to pre monsoon seasons (September to November) and shows the negative gradient for most of the altitude. The RR and LWC show the opposite characteristics, and both have a positive gradient below the 6 km altitude and then negative gradient above 6 km altitude. The raindrop size distribution (DSD) parameters show most of the variation below the freezing level, and a higher concentration of large sized of hydrometeors are observed for higher RR, however the dominant modes of D_m are less than 1 mm. The changes in the VSR in DSD parameters are significant for the RR>20 mm/h, whereas for RR<2 mm/h the vertical structure in DSD parameters do not have much differences during monsoon and pre monsoon seasons. Satellite and reanalysis data reveal the short periods of convective activity with higher accumulated rainfall over HYO compared to stratiform precipitation, which is more common in the nighttime and sustain for many hours. Wet spells (higher rainy days) have low pressure circulation, which favours the transport of moisture from the Amazon to the central Sierra of Peru, while the anticyclonic circulation at high levels favours the divergence at higher pressure levels and, enhances the convective in the region. During the dry spells, low level weaker circulation at the west of Brazil, restricts the transport of moisture to the central Sierra, while the circulation at high levels does not favor rain processes. The improved understanding of the tropical Andes precipitation would be very important for assessing climate variability and changes as well as to forecast precipitation using the numerical models.

Keywords: MIRA35c; diurnal variation; DSD parameters; convective rain and bright band

1. Introduction

Peru is known as the country with natural hazards, where these natural hazards affect the social and economic life within the valley of Andes. The west coast of Peru consists of dry Pacific Ocean, whereas at the interiors it is divided by the Andes mountain, and east of Peru has a large area of Amazon forest. The mountain area covered by Andes with its complex topography makes very difficult to measure the correct rainfall estimation from the satellite-based observations due to attenuation in the precipitating media [1]. At the same time, numerical models are not able to track and forecast precipitation properly [2-4]. More recent research work over the tropical Andes revealed that precipitation in tropical high mountains occurs due to a complex interaction of atmospheric processes and external factors on several scales [5-9]. Mantaro Basin (MB; Fig. 1a) is located in the valley of the Andes mountain and known as to have some severe thunderstorms during to September to March months [9-10]. There are not much information's are available about the vertical structure of rain (VSR) and raindrop distribution (DSD) due to unavailability of ground-based observations in the complex valley of Andes. In 2015 the Instituto Geofísico del Perú (IGP) started the ground-based observations to investigate the various characteristics of rainfall including diurnal cycle, VSR, and DSD parameters within the valley of Andes. As a part of it, a vertically pointed profile radar (VPPR, Fig. 2), namely MIRA35c is installed at Huancayo (HYO, 12°S,75.3°W) to investigate the rainfall characteristics. Also, an intensive field campaign took place at HYO between 18 February to 19 March 2019, and the results from the field campaign are presented here.

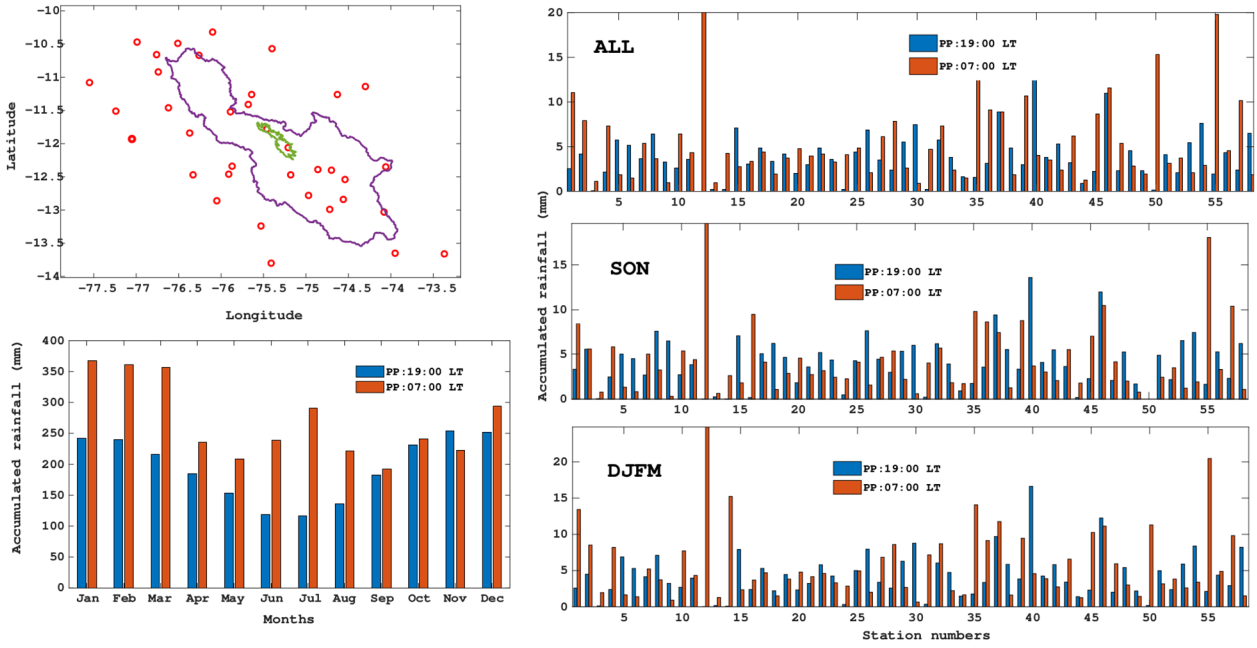

Figure 1. Rain gauge observation of the diurnal cycle of surface precipitation (a) rain-gauge network marked by red circle and boundaries are showing the boundary of Mantaro basin and valley (b) Monthly variation of accumulated surface rainfall at 07 and 19 local time for all the rain-gauge stations (c) accumulated surface rainfall at 07 and 19 LT for all the stations for all the day of the years, (d) same as c but for September to November months (e) same as c but for December to March months.

Figure 2. (a) Locations of MIRA35c (b) images of MIRA35c.

The diurnal cycle of rainfall over the tropical high mountain and its mechanism of formation are discussed earlier [e.g.11-13]. For example, in an early work, it is observed the diurnal patterns with higher rainfall between the altitude 2600 and 3300 m mean sea level (msl) over eastern cordillera of the tropical Andes, with higher nighttime rainfall [14]. Over the last two-decade satellite-based observations mainly based on Tropical Rainfall Measuring Mission Precipitation Radar (TRMM-PR) and Global Precipitation Measurement (GPM) provide the diurnal cycle variation over the different regimes of South America (SA) and Andes mountain [13,15-16] and the vertical structure of rainfall (VSR) over the tropical globe [17-22] included land and oceanic regions over the South America [15-17,23-25]. But there are several limitations on the satellite-based observations. First, TRMM/GPM is non sun-synchronous satellite width swath width of ~247 km, and not able to capture otal and complete rainy events over specific areas/location. Second, it has much higher sensitivity (~17 dBZ), and not able to capture the light rain and drizzle. Also, the lack of DSD parameters could influence its outcome [26-28]. For example, it is mentioned that TRMM underestimates more than 50% stratiform rainfall below the TRMM sensitivity [29]. Ground-based observations could lead to a better understanding of the VSR characteristics, although they also showed the uncertainty in rainfall [26-27, 30]. DSD plays a vital role in tropical rain and cloud system [31-35] and its variation affects the VSR because of several microphysical mechanisms. For example, evaporation, break up, collision-coalescence affects the near-surface DSD, which leads to variation in the VSR. The major source of uncertainty is the variation near the melting layer/height [36] and the humidity structure in the lower troposphere [37]. For example, the constant reflectivity assumption from the surface to melting layer affect the variation in VSR and thus it is very important to investigate the BB characteristics [36].

There are very few studies, which reported the vertical variation in radar reflectivity (Z_e) with the change in DSD spectrum with the height and their influence on rain rate (RR)[26,28,36,38,39] and seasonal variation in Z_e-RR relationship using the ground-based DSD measurements [31,40-42]. For example, Peters et al. [26] showed the change in the DSD parameters with Z_e-RR relationship in the Baltic during heavy rainfall and showed that DSD parameters depend on the RR. Thurai et al. [27] also showed that strong variation in VSR in convective and stratiform rainfall in Singapore region. Das et al. [36] observed the VSR characteristics over the three tropical regions over South Asia. They showed that negative slope in the raindrops below the melting layer height for RR greater than 20 mm/h. At the same time, RR less than 2 mm/hr has a much higher fraction of small drops below the 1 km altitude. Sumestha et al. [39] observed the BB characteristics and microphysical processes in the stratiform precipitation over the Western Ghats over India and found that 60% of the BB lies nearly at 4.6 km altitude. In mid-altitude cloud the DSD shows the bimodal distribution for the lowest class of the RR ($0.1 \leq RR < 1$ mm/h) whereas for high-altitude clouds the DSDs do not show any modal

distribution and does not depend on the rain categories. They also showed that DSDs parameters in BB events show the concave downward shape near the surface levels due to collision-coalescence processes in the mid-altitude clouds. Schuur et al. [43] showed that major variability in DSD parameters is associated with the stratiform rain with low intensity and in the advance of convective rains. The limited studies are available over the Andes, which showed the VSR observation along with the diurnal cycle of precipitation events over the tropical Andes [44-46]. Perry et al. [47] investigated the characteristics of precipitating storms over the Glacierized Tropical Andean Cordilleras of Peru and Bolivia using vertically pointing MRR. They showed the dominance of nighttime higher stratiform precipitation and showed that rainfall in the valley of the Andes results from the interaction between easterly moist flow and westerly flow at the different pressure levels. Endries et al. [46] used MRR data over the Andes mountain and showed higher RR in the afternoon and overnight time with short periods of strong convective cells.

From the past study, it is clear that in a mountainous region, the interaction between the wind systems and complex topography can affect the precipitation processes [35,48]. Also, from light to heavy rain, raindrops undergo several microphysical processes at different altitude and then reaches at the surface [49-52]. The dominant microphysical processes such as coalescence, collision, breakup of raindrops are complex microphysical process and represent the uncertainty in numerical models [53]. Therefore a climatological and filed campaign analysis of the rainfall, BB and DSD parameters at the terrain conditions are essential to make a holistic understanding of the processes and to formulate the parameterization of precipitation in weather and climate models [2-4,9]. At the same time, it could be very useful for getting the positive results in cloud seeding experiment [54]. However, this is a very first attempt to characterize the growth and evolution of the vertical DSD structure in relation to mean VSR over the complex topography of Andes. The present analysis also examines the microphysical processes associated with the convective and stratiform rainfall over the HYO. In summary, a statistical analysis of the diurnal cycle, BB and VSR obtained from VPPR over HYO for 3 years (2015–2018) of the data. In summary, the main objectives of the present study is to address the following questions:

1). How do the diurnal cycles of rainfall vary over the tropical Andes?

2). What are the associated spatial and temporal distributions of BB heights?

3). How do the vertical structures of rain look like for a specific rain rate and drop size vary over Huancayo, Peru?

4). How do the rainfall patterns look during the campaign over the Huancayo? Following paper is organized as follows.

Section 2 provides rainfall climatology over the tropical Andes, and section 3 provides detailed information about the MIRA35c and other data used in the present study. Section 4 provides the results and discussion from the study, and section 5 concludes the study.

2. Precipitation climatology over the Andes mountain

The rainfall over the tropical Andes is associated with the upper-level Bolivian high (BH, counterclockwise circulation) during austral summer (December to March) monsoon [55] and the rainfall in the valley is affected by the influence of mountain-valley circulations due result of thermal differences [56]; On the other hand, BH weakens from May to October [57]. The low-level jet (LLJ) and surface flow play an important role and transport the moisture flow from Amazon to Andes and affect the DSD parameters at low lands and eastern slope of the Andes [35, 57]. A meso-scale cloud systems show the bimodal distribution of diurnal patterns, and peaks occur in the overnight and afternoon hours over the Andes mountain [13,15,45,58,59-60]. The rainfall within the valley shows a clear afternoon peak in many studies and other parts of the Andes [13,15-16,35]. GPM data revealed that near surface rain properties such as RR and DSD parameters depend on the topography and surface wind directions [35] whereas the higher frequency of MCSs is observed at the eastern flank of Andes [60]. Sulca et al. [61] showed the role of large-scale circulation on the dry and wet spells over the MB and revealed the necessity of upper-level circulation for triggering the rainfall over the MB. A seasonal marked behavior is also observed as the peak of accumulated rainfall found between

austral summer (DJFM), and then September to November (SON) seasons [10]. On an average, for the entire valley, there is marked seasonal variability in rainfall, with maximums rainfall between January and March and minimums between June to July [10]. It was found that 83% of the annual rainfall takes place between October to April, of which 48% are distributed almost equally between January, February to March. Moreover, the trade winds from north-east are intensified and transport moisture into the continent [62] and these winds cross the Amazon basin and rise on the Andes mountains, and contribute to rainfall [63].

A dense rain-gauge network over MB are shown in Fig 1a, and the red circles show the locations of the rain-gauge stations over the MB. SENAMI (National Meteorology and Hydrology Service of Peru) provides the surface rainfall for every 12 hours accumulated rainfall; e.g., at 07 local time (LST; 12:00 UTC) in morning and afternoon (00:00 UTC; 19 LST). In that sense, it provides a diurnal variation of the surface rainfall over the MB, and nearly 38 years (since 1981) of rainfall data are used in the present analysis. Figure 1b shows the monthly variation of the accumulated rainfall at 07 (00:00 UTC) and 19 LST (12:00 UTC) over the mentioned stations. A hint of the diurnal cycle is observable and, for most of the months (except November), night-time accumulated rainfall is higher compared to day time accumulated rainfall and consistent with the past finding [14] and satellite-based observations [13,35,45,47]. Fig 1c-e shows the accumulated rainfall for 12 hours for all years, DJFM and SON seasons at 07 and 19 LST at different stations. It also shows a clear hint of diurnal variation for most of the stations. For most of the rain gauge stations, the night time accumulated rainfall is higher compared to day time of the rainfall. Based on the monthly rainfall climatology/variation [10], we chose two seasons, namely monsoon (Austral summer) and pre monsoon season (SON) for the further investigation of rainfall characteristics over HYO.

3. Data and Methodology

We used the ground-based VPPR, namely MIRA35c working at 24.1 GHz with the other reanalysis data and mentioned below. Also, the methodology used in the present study is mentioned below.

3.1. The Compact Meteorological Ka band Cloud Radar (MIRA-35c)

The VPPR is placed in the HYO, located in the center of the MB (Fig. 2a). The MB is located in the central Peruvian Andes (10◦34'-13◦35'S, 73◦55'-76◦40'W) with an area close to 34550 km^2 (Fig. 1a). Figure 2 shows the location and image of the MIRA35c, which measures clouds and rain. MIRA35c is a magnetron based pulsed Ka-band Doppler radar, with very high sensitivity and ability to detect the clouds and fog. MIRA35c transmits the linearly polarized signal and receives co and cross signals simultaneously, to detect the Doppler spectra of radar reflectivity (Z_e) and the Linear De-polarization-Ratio (LDR). Both the data are used to investigate the cloud density and target type respectively [64]. Its ability to detect the cloud and rainfall and work as a bridge between the gap in Earths hydrological cycle by adequately detecting clouds and precipitation and showed in many studies. MIRA35c is specially designed radar and most compact cloud radar available today, and the low power consumption makes it perfect for automatic measurements at remote locations. To derive the vertical velocity, Z_e, RR and DSD parameters from the MIRA35C, we used the algorithm used in [26,36]. Table 1 shows the variables and description of the MIRA35. Figure 3 shows an example of the vertical profile of Z_e and vertical velocity measured through MIRA35c. From the figure, it is clear MIRA35 can measure convective and stratiform rainfall events. For example, Fig. 3a and 3c are showing the convective rainfall events with Z_e>35 dBZ from the surface to mixed phase altitude, whereas Fig. 3b and 3d showing the Z_e structure with BB events and indicate the stratiform rainfall events.

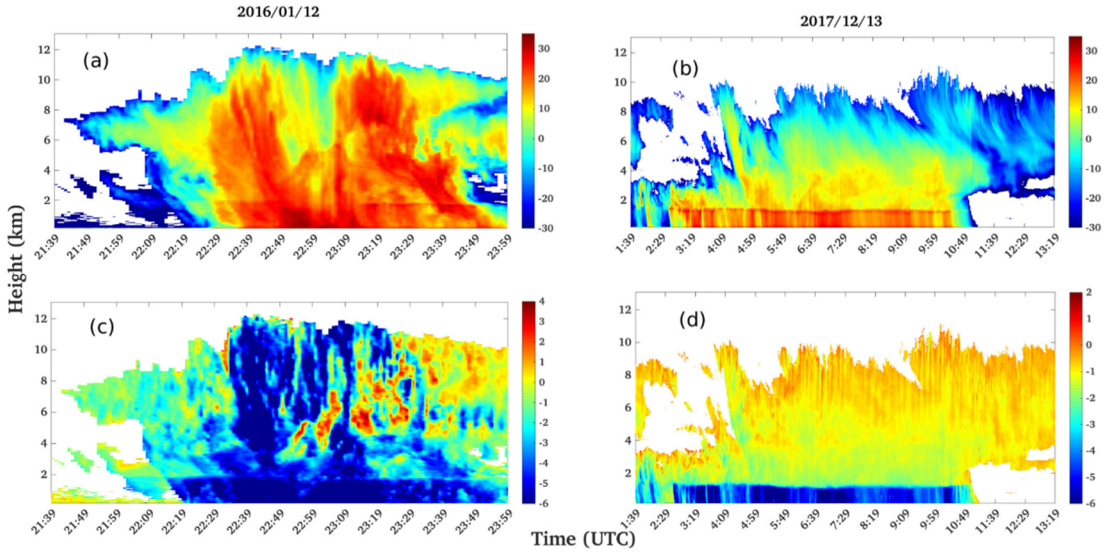

Figure 3. An example of radar reflectivity in convective (a) and stratiform (b) and vertical velocity in convective (c) and stratiform (d) rainfall events on 29 December 2015 (convective) and 13 February 2017 (stratiform) rainfall.

Table 1. Some Important Specifications of the MIRA35c.

MIRA35c Specifications				
Frequency	**Peak Power**	**Receiver**	**Operation mode**	**Beam width**
34.85	2.5 kW	Single Polarization	Pulsed	0.6^0
Antenna type	**Range resolution**	**Temporal resolution**	**Number of range gates**	**Number of spectral bins**
Cassegrain	31 m	5.6 s	415	128

3.2. BB height estimation

The BB height is calculated vertical Z_e profiles using the algorithm mentioned in [65, see Fig.3] and the negative gradient in Z_e profile is used to find the BB height [46,65]. We removed the virga rain from the study, where rainfall does not reach the surface. For the vertical profiles which consist of BB, the height consists of maximum Z_e (Z_{emax}) is termed as H_{peak}. The BB top height (H_t) is defined as the height consists of the highest negative gradient of Z_e, whereas BB bottom height (H_b) consists of the largest positive gradient of Z_e. This methodology is different from the methodology used X-band Doppler radars, i.e., the SNR (Signal and Noise Ratio), falling velocity, and reflectivity [66]. We also defined reflectivity of snow (Z_{esnow}) and rain (Z_{erain}) defined as the Z_e at 150 m above H_t and below H_b, respectivel.

3.3. Vertical structure of rain (VSR) at different rain rate

VPPR data is validated in the past over different part of the globe and rainy areas [26, 33-34, 41-42, 67], and results showed the VSR depends on the DSD parameters. For studying the mean VSR, we followed the methodology described in [26,36]. We divided the near-surface RR into four categories, namely 0.02–0.2 mm/h, 0.2–2 mm/h, 2–20 mm/h and 20–100 mm/h [36]. The basic regions behind this classification are that RR could classify the rain into convective and stratiform [26,36]. There are various studies which used the various methodology to separate the convective-stratiform rain based on the BB [68], however, RR is commonly used to discriminate the convective-stratiform

rainfall because of its simplicity [26,36]. Ground bases observations revealed that near-surface DSD measurements can differentiate between convective and stratiform rainfall [31-34]. However, this is a very first approach in the valley of Andes to investigate the vertical growth and evolution of DSD structure in VSR. For this purpose, we include in the statistics only the rain profiles which reach to the lowest range gate of VPPR nearest to the ground. In averaging the data set, there are still some possibilities of suppression of information. Peters et al. [26] showed that this suppression of information is not very serious, and the mean dataset can still efficiently serve the purpose of the study. For understanding the rain structure over HYO, we study the profiles of RR, liquid water content (LWC), and Z_e for different near-surface RR as discussed earlier during DJFM and SON seasons.

3.5. Campaign and reanalysis data

A short but intense field campaign is launched over HYO between 18 February to 14 March 2019. Several ground-based instruments including radiosonde, ground-based radar and Boundary Layer and Troposphere Radar (BLTR), are used to investigate the rainfall and mechanism behind it over HYO. We used the reanalysis data from the GFS at 1° x 1° grid resolution including variables wind velocity and wind direction at different pressure levels to investigate the evolution of clouds during the convective and stratiform precipitation events. We also used the ERA-interim data for Geopotential height and specific humidity at 1° x 1° grid resolution to investigate the dynamical behavior of rainfall during dry and well spells during the campaign periods. We also used the Geostationary Operational Environmental Satellite (GOES) satellite data which provides brightness temperature (BT) to see the evolution of the cloud systems. The spatial and temporal resolution of GOES satellite is nearly 4 km and half an hour respectively.

Table 2. Summary of the data sources.

Source	Variable	Temporal Scale
VPPR, Huancayo	Radar reflectivity, echo top height, DSD parameters bright band height, Rain rate (2015-2018)	1 min
Rain gauge	Precipitation (1981-2019)	1 min
Radiosonde	Temperature and humidity (February-March 2019)	Instantaneous
ERA-Interim ECMWF	Upper level winds	6 hour

4. **Results**

4.1. Rainfall variability and diurnal variation of the surface rainfall

Figure 4 shows the diurnal cycle of surface rainfall observed from the MIRA35 during the study period e.g., DJFM and SON months. The seasonal differences are less and all the panels reflect the diurnal variation and mean RR (mm/h) and maximum of mean RR follows the diurnal patterns and consistent with the different locations of Andes mountain (southern Ecuador; [13,46,60]. The diurnal cycle during the study period shows the two maxima in RR, namely afternoon [17:00 to 19:00 LST] and then after midnight hour [1:00 to 3:00 LST]. However, the mean of maximum RR shows several maxima during the study periods. DJFM and SON also follow the similar trends, however, the mean RR is higher during SON (~0.4 mm/h) compared to DJFM months (~0.35 mm/h). The two major differences are observed during two seasons, namely between the magnitude and temporal distribution of maxima of mean RR. The difference between afternoon and mid-night maxima is higher during SON compared to DJFM and shows most of the rainfall maxima occurs in afternoon, and could be related to more topographical condition rather than the DJFM seasons, where meso-scale dynamics and diurnal heating both are important [9]. For example, the mean RR peaks at ~0.35

mm/h and 0.18 mm/h for afternoon and early morning during DJFM months, whereas corresponding values are ~0.4 mm/h and ~0.05 mm/h for afternoon and midnight peaks for SON seasons. Second, the DJFM shows a clear maximum at 18:00 LST, and, then decreases around 18:00 LST, whereas maxima in mean RR spread between 15:00 to 18:00 LST during SON months. The mean of the maximum RR also shows the similar trends, and the difference between afternoon and early morning mean in the maximum RR is less for JJAS months (~2 mm/h) and highest during SON months (~8 mm/h). Figure 5 shows the diurnal cycle of accumulated surface rainfall and maximum accumulated surface rainfall at each half an hour interval during the study periods, DJFM and SON months. SON has a clear pattern of the diurnal cycle compared to DJFM months, where the maximum accumulated rainfall occurs at 13.00 LST and then decreases around the mentioned time. SON has a clear maxima in afternoon and midnight hours and the observed bimodal distribution of precipitation is consistent with the past results [45-47] and reflects the night-time and widespread precipitation over the nearby areas.

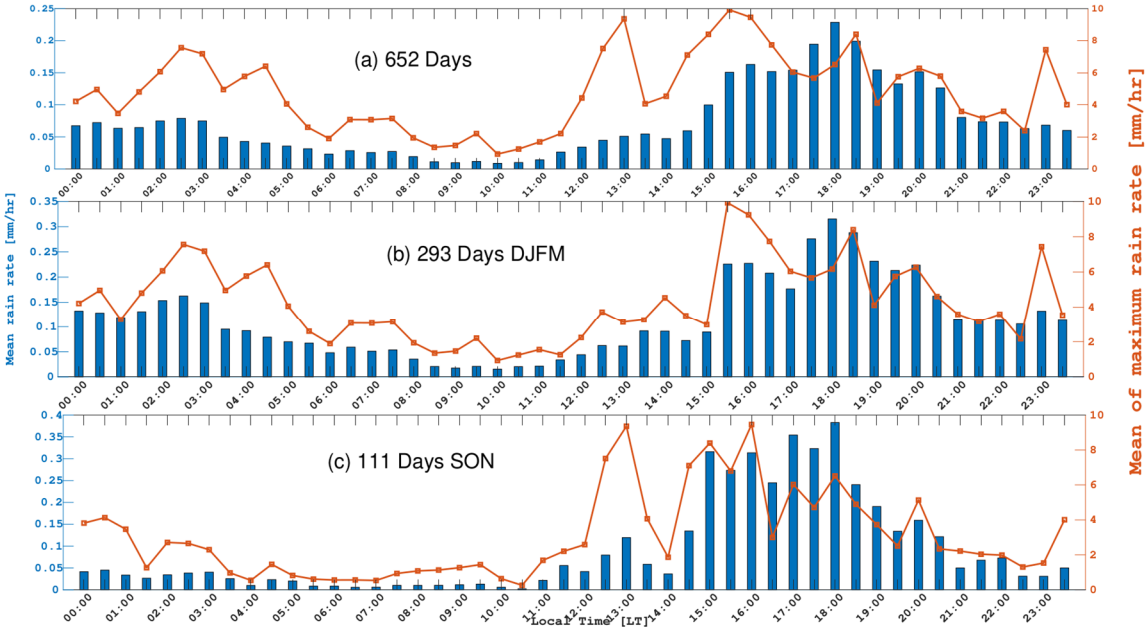

Figure 4. Time series of the mean rain rate (mm/h) and mean of the maximum rain rate (mm/h) for (a) all the study periods (b) December to March months and (c) September to March months observed from MIRA35c.

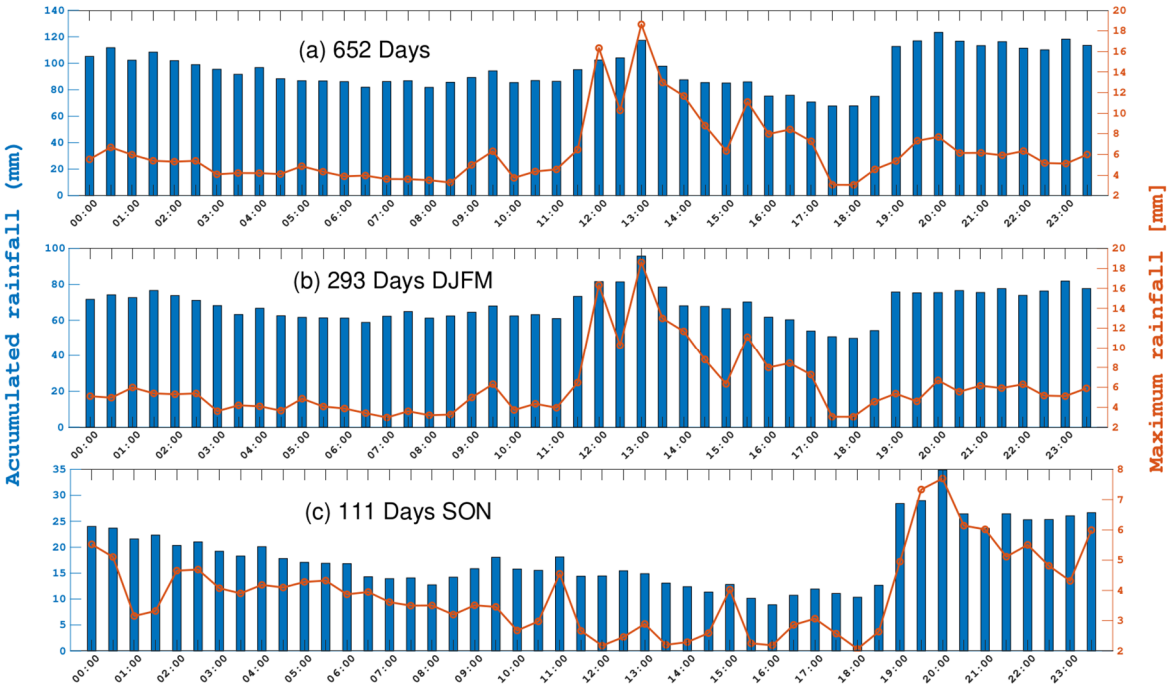

Figure 5. Time series of the accumulated rainfall (mm) and maximum rain fall at particular rime (mm for (a) all the study periods (b) December to March months and (c) September to March months observed from MIRA35c.

4.2. Bright band characteristics

Figure 6 shows the diurnal variation (a-c) and probability density distribution (d-f) for BB height observed during two seasons and whole study periods. It is important to observe that BB is higher during summer monsoon season compared to pre-monsoon seasons (SON months). The probability density distribution of BB shows the seasonal variation and the DJFM months have the two peaks (4.4 and 4.6 km), whereas SON has a single peak near 4.5 km altitude and the maximum height of BB lies between 4.2 to 4.6 km altitude. The probability of BB height decreases sharply after 5 and 4.7 km during DJFM and SON seasons respectively. The BB height mostly lies between 4 to 5 km altitude and consistent with the other stations/locations over the Andes mountain [46-47]. However, irrespective of diurnal cycle more than 70% of BB lies nearly well below the 5 km altitude, and only less than 20% BB found over 5 km altitude and even higher in nighttime. The BB height clearly shows the diurnal patterns and role of solar heating at the higher topographic areas. First, the higher density/frequency of BB with high altitude (4.5<BB<5) occurs either afternoon or evening (13:00 LST to 21 LST) and other maxima occur between 22 LST to 6 LST, but BB is mostly less than 4.5 km. Although, there is a possibility that BB could rise more than 5 km, mostly in afternoon and late night (13:00 LST to 23:00 LST), and follows a heating pattern over the tropical Andes and lead to higher BB [65]. Table 3 provides the detailed information of BB observed during the different periods of the time. The seasonal differences are not very pronounced but the diurnal variation evident and shows the variation of 500 to 900 meters. For example, mean BB is highest (~4.66 km) during SON months between 14:00-19:00 LST followed by DJFM months (4.62 km) between 20:00-01:00 LST. Although the highest median BB (~4.57 km) height found between DJFM months during 20:00 to 01:00 LST and the standard deviation in BB height is higher during SON months compared to DJFM months.

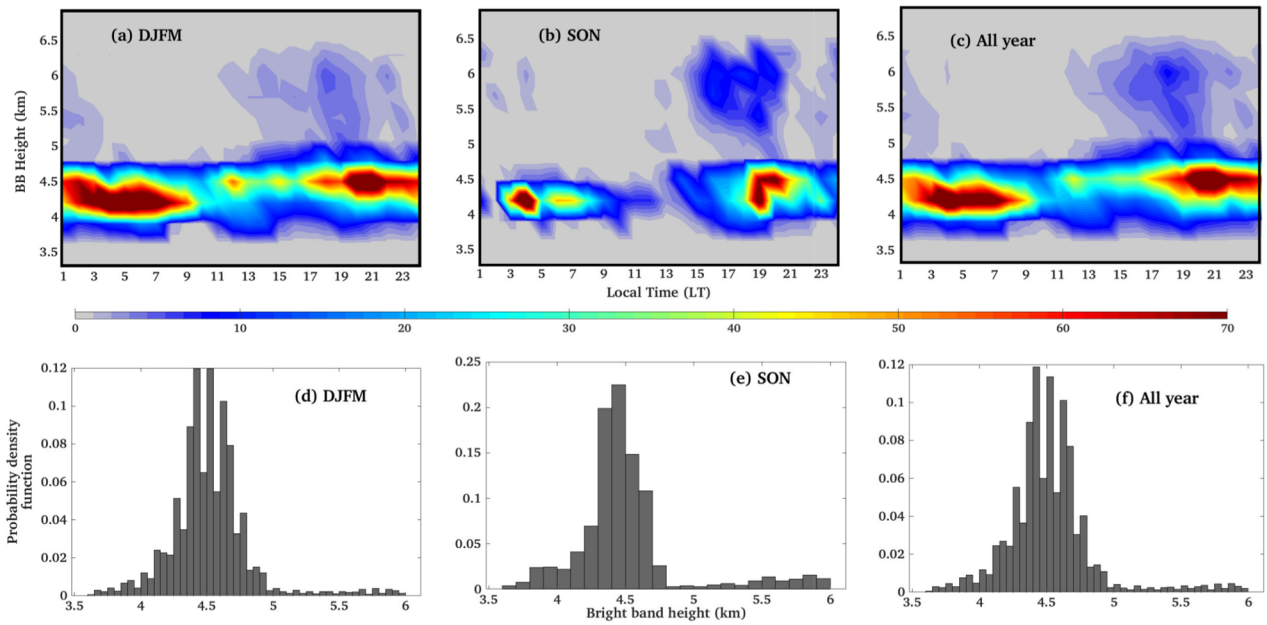

304

305 **Figure 6.** (a) Time series of the bright band altitude for the Austral summer monsoon season
306 e.g., December to March months (b) same as a but for September to November months (c)
307 same as a but for all the study periods. (d) Probability density function (PDF) of bright band
308 height for December to March months (e) same as d but for September to November months
309 (f) same as d but for all the study periods.

310 **Figure 7.** shows the scatter-plot for the Z_{epeak} and Z_{erain} for different RR for the vertical profiles
311 consisting the BB. Both the seasons nearly show the common trends and for higher near-surface RR
312 (>1.5 mm/h) has a linear relationship between Z_{epeak} and Z_{erain}. The role/effect of the melting layer and
313 BB are evident and shows the conversion of ice or frozen hydrometeors into the rain droplets below
314 the melting layer [69]. The BB features is an important integral of stratiform precipitation and
315 whenever ice particles fall from the cloud tops or in their downward journey they grow by the
316 deposition of vapor into large sized of hydrometeors [70]. Once they enter the zone of within the 2.5
317 km of the freezing level, aggregation and riming formed the irregular shaped of snowflakes; which
318 melt at 0°C isotherm and produced the BB [71-74]. .

319 **Table 3. provides detailed information of the BB height within the different diurnal**
320 **times.**

	Midnight		**Afternoon**		Overnight	
	13:00 – 18:00 UTC **8:00 - 11:00 LT**		**19:00-00:00 UTC** **14:00-19:00 LT**		01:00-06:00 UTC 20:00-01:00 LT	
	DJFM	SON	DJFM	SON	DJFM	SON
Number of Profiles	(11976)	(1523)	(11976)	(1523)	(11976)	(1523)
Max	6.44	6.41	6.38	6.41	6.47	6.47
Min	4.01	4.10	4.01	4.04	4.01	4.01
Median	4.47	4.32	4.41	4.38	4.57	4.50
Mean	4.52	4.43	4.44	4.66	4.62	4.32

Standard deviation	0.306	0.426	0.255	0.281	0.339	0.49

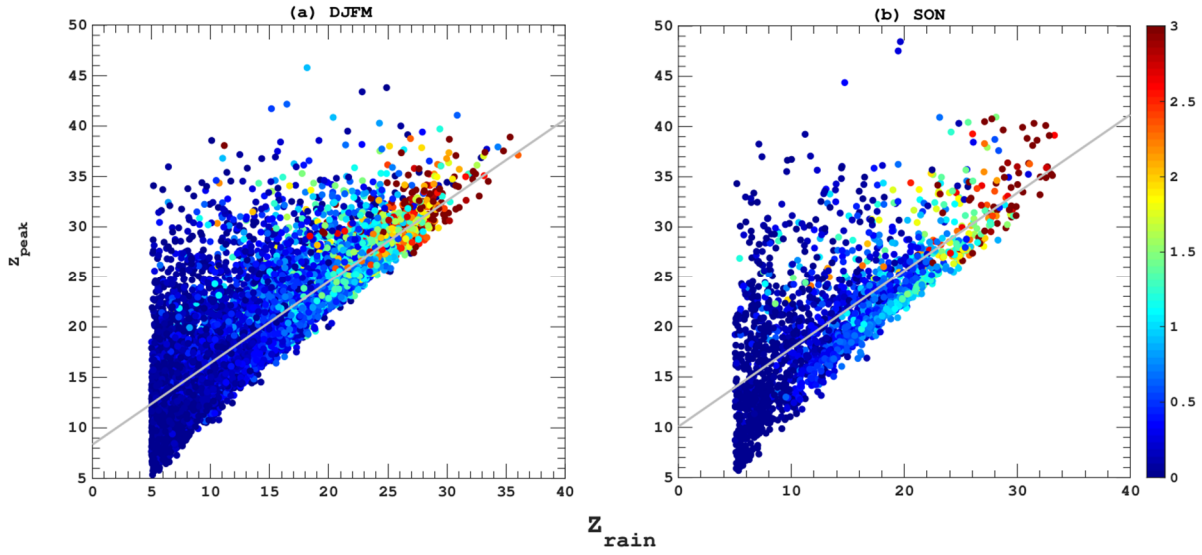

Figure 7. Scattering plot between Zerain and Zepeak as a function of rainrate.

4.3. Vertical structure of rain

Figure 8 shows vertical variation of Z_e, RR and LWC (gm^{-3}) for DJFM (solid line) and SON (dot-dash line) months and the seasonal differences are observed and monsoon seasons have the intense vertical profile compared to pre-monsoon months except for the RR for class IV (RR>= 20 mm/h), wherein the mixed-phase altitude (6-9 km) the average Z_e is higher in SON months compared to DJFM months. The maximum differences in Z_e profiles are observed between the mixed-phase height, and above the 9 km; the average Z_e profiles merge and consistent with the longterm TRMM and GPM observations for the intense rainfall events over different part of the globe and nearby areas of South America[17,20,23-24,75]. The BB signature is absent in most of the average Z_e profiles and they are showing the negative slope with height and average Z_e decreases with the height. The average vertical profiles of Z_e can be divided into two regions, one below ~5.0 km (very near to 0°C; Fig. 8a), where average Z_e either increases, decreases or remain constant with the height, and depends on the class of RR, whereas above 5 km, average Z_e decreases with the height for all class of RR. Within the lowest ~1 km altitude, the average Z_e is highest for RR between 20 to 200 mm/h and least for RR lies between 0.02-0.2 mm/h. Above the BB height (~4.7 km) average Z_e profiles show the different characteristics, and the average Z_e is least for classes of RR of class IV (20-200 mm/h). The average slope changes in the mixed-phase regimes and related to the growth and decay of the hydrometers in the evolution of cloud/rain droplets and depends on the cloud microphysical processes [70]. Figure 8b shows the average vertical profile for RR for different classes of RR (I-IV) and again the seasonal differences are observed and monsoon seasons are more intense compared to pre monsoon seasons except for class of IV RR (>20 mm/h) above 4.5 km altitude. It is important to see that x-axis is in logarithmic scale. For the near surface RR <= 2 mm/h, average RR has positive slope e.g., average RR increases up to 6 km altitude and then decreases slowly or remain (negative slope) constant and in accordance with the past studies over the different part of globe [26-27,67,76]. SON shows the different characteristics compared to DJFM months for RR (20-200 mm/h) and the reason is not clear. Maybe the mixed rain, during the transition from convective to stratiform rain, where local convection or convective systems could become stratiform precipitation very quickley [36]. The moisture transported in upslope and easterly flow generates the higher near surface RR and large sized hydrometeors at the eastern flank of the Andes [35]. The rising moist air flow along the slope, it condensates and starts falling down and increase the local precipitation [48]. The opposite slope below the ~4.5 km altitude for RR below the 2 mm/h, reveals that hydrometeors generated near the freezing level are able to reach the surface and evaporation of small hydrometeors are effective

in lowest class of RR and shows the role of moisture availability and water vapor in the regions during Austral summer monsoon seasons [9,15]. Figure 8c shows the vertical variation of LWC for the different classes of RR and shows similar patterns as observed in average RR profiles and monsoon months have higher LWC compared to pre monsoon months. For the lowest class of RR (<0.0-0.2 mm/h) the LWC has a positive slope (dLWC/dz>0) up to 6 km altitude similar to RR profiles and then remain constant or consists of negative slope. Again the average LWC is least for DJFM months above 4.5 km altitude and similar to that observed in RR and Z_e profiles for RR>20 mm/h. For the RR of class IV (RR<20 mm/h), average LWC has a positive slope (dLWC/dz>0) from the surface up to 6 km altitude. These findings are consistent with the higher altitude regimes over the Shillong (~1.6 km) over Indian subcontinent [36]. The negative slope for higher RR is expected and the errors introduced by an overcompensation of the rain attenuation at high RR as mentioned in [36]. However, the positive slope in the LWC shows the correct estimation and errors are very less in this RR range due to rain attenuation. The possible regions behind such kind of behavior are the shift of the DSD peak and DSD peak toward smaller drops with increasing height. The lowest class of RR generally associated with the drizzle (with Z_e<0 dBZ) and related with the lower shallow clouds and with less fall velocity and smaller drops and also showed in next section [26,76]. At the same time, evaporation plays a significant role at very low RR and lower height and affects the small drops concentration and lead to the positive gradient in LWC and RR vertical profiles below the 6 km altitude.

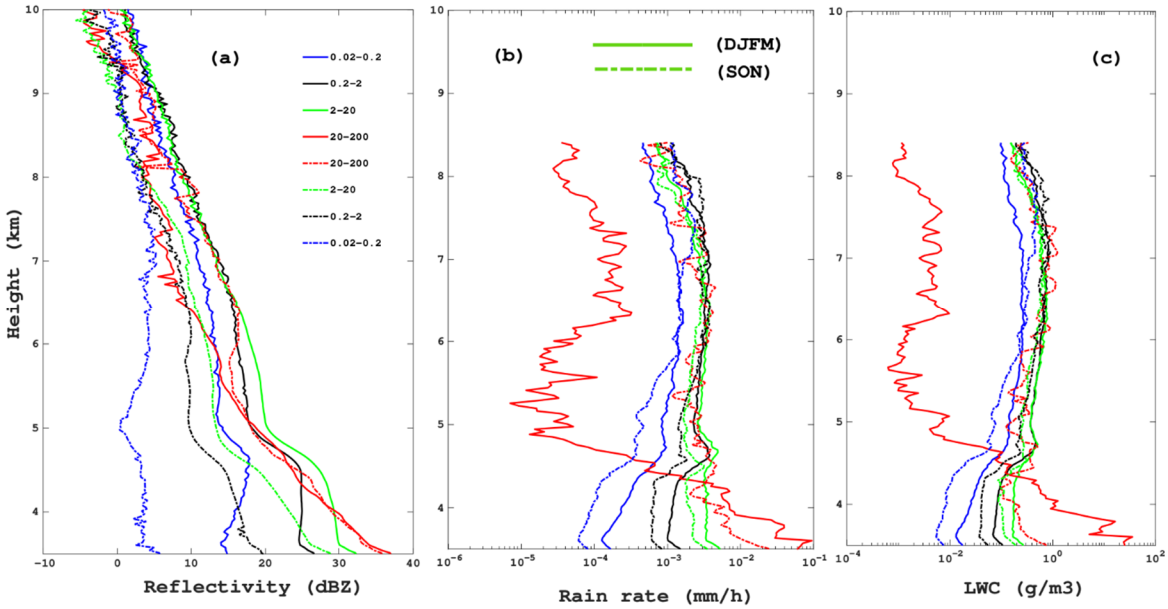

Figure 8. Average vertical profile for different class of rain rate for December to March and September to November months for (a) radar reflectivity (in dBZ) (b) rain rate (mm/h) and (c) liquid water content (g m^{-3}).

4.4. Distribution of drop size parameters Mean drop size distribution and drop evolution mechanism

Figure 9 shows the vertical profile of the mean DSD, obtained from MIRA35c for four classes of RR (I-IV). We plotted the DSD vertical growth up to ~8 km, but will discuss mostly below the 6.5 km altitude e.g. nearly above and below the freezing level (Fig. 5). The vertical DSD growth during pre monsoon and monsoon months show nearly the similar characteristics with minor seasonal differences below the freezing height (Fig. 9). In general, all classes of RR are showing the similar trends of higher/bigger raindrops near the surface compared to high altitude regimes. The seasonal differences are evident as DJFM months have a higher concentration of bigger drop for less RR. Below we will discuss in details about the DSD vertical growth for the four class of RR. For the lowest

class of RR (0.02-0.2 mm/h) , the D_m<1 mm shows the higher concentrationand dD/dZ remains constants below the freezing height, but the drops less than 0.5 mm shows the opposite characteristics during JJAS and SON seasons. For example, in a small differences for the lowest RR class the raindrop less than 0.5 mm, shows the negative trends (dD/dZ<0), just below the freezing level during SON season, and indicates the drop break up or evaporation mechanism, but not very frequent during DJFM months and this could be because of the sufficient moisture supplied by the SA-LLJ. Although the total number of smaller drops (D_m<1.0 mm) remain constant within the mixed-phase regimes and increases below the freezing level during both the seasons. This indicates the evaporation of small drops (0.5 mm-1.0 mm) does not affect the much rainfall over HYO. The higher concentration of bigger raindrops below the freezing height because of moisture loaded surface flow under the orographic influence. This indicates that the sufficient moisture loaded flow through South American low-level jet (SA-LLJ) under the orographic influence provide enough moisture to overcome the evaporation effect. The negative gradient into the small droplets is consistent with the past studies over the high altitude areas of the Western Ghats (WG) over South Asia.

For the RR lies between 0.2-2 mm/h, the DSD parameters show the dominance of drop collision-coalescence mechanism during both the seasons and a higher concentration of bigger raindrops (D_m>1 mm) are observed below the freezing level during both the seasons. Although overall DJFM months consist of higher concentration of higher-sized of raindrops compared to SON months. The concentration of the smaller drops (D_m<1 mm) also shows the similar characteristics and increases in the lowest height. Although in a small difference, SON months show the decrease in the concentration of D_m<0.5 mm and indicate the hint of the evaporation of the small drops. For the RR lies between 2-20 mm/h, the seasonal differences are higher compared to lower classes of RR, although the DSD variations are same in both the seasons. During both the cases, higher concentration of larger raindrops (D_m>4 mm) are reaching to surface compared to previous cases. Since the mentioned RR consists of both convective and stratiform precipitation, both the drop evolution mechanism, namely collision-coalescence and break up are effective. For RR class between 20-200 m/h a higher concentration of rain drops of D_m<= 2 mm are observed between the mixed-phase regimes. The role of evaporation and orographic wind is evident as most of the small rain drops are removed from the location due to strong wind. At the same time, the concentration of bigger raindrops is also higher near the surface compared to other class of rainfall. Since this class of rainfall mostly correspond to convective rainfall and consist of the evolution of bigger raindrops near the surface. At the same time, it also shows the higher concentration of bigger raindrops throughout the height regions compared to other class of rainfall. The observation indicated that there are much higher chance of collision-coalescence in the lower altitude, whereas in the ice microphysics are

responsible for bigger raindrops within the mixed-phase regimes [36].

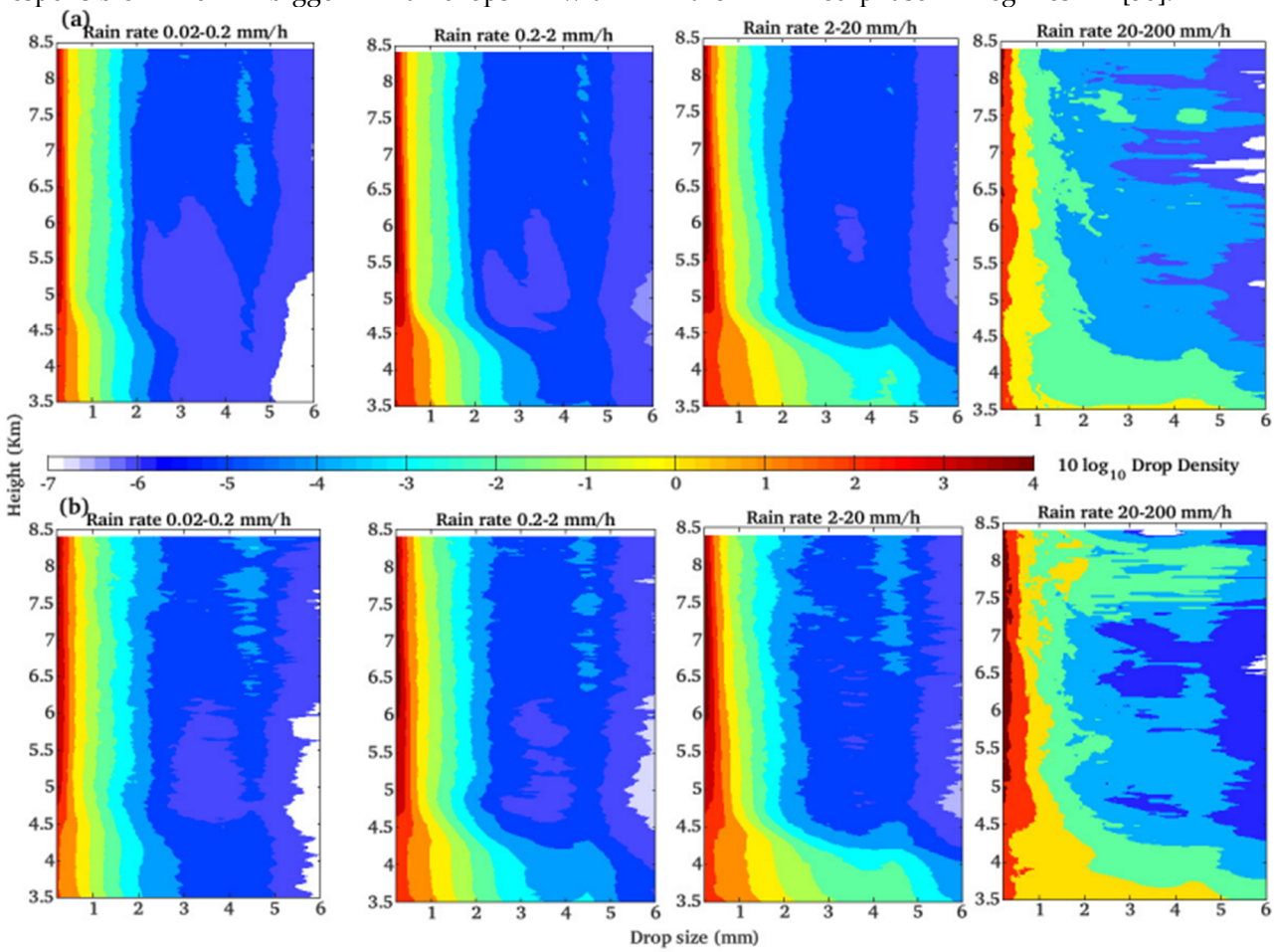

Figure 9. Average vertical DSD profiles for (a) December to March months and (b) September to November seasons. Different DSD figures in each panel correspond to the rain rates ranges as indicated in previous figures.

HYO is at 3.2 km above msl and very near to the BB height and once the snow or ice crosses the 0°C height, it melts and creates the bigger raindrops, which falls quickly. In a recent study, Gatlin et al. [77] used ground-based radar data and showed that a thickening, and to a lesser extent a lowering, of the BB causes an increase in raindrop diameter below the BB that extends to the surface. At the same time strong orographic wind could leads to small drops to a higher altitude, and we can see the negative slope. Raindrops often develop from the melting of precipitation-sized ice hydrometeors [78]. For example, melting snowflakes are a common source of rainwater in stratiform precipitation. Several studies have found that larger raindrops were observed at the ground beneath more intense radar reflectivity BB. The constant cloud base layers due to supplied moisture within the boundary layer affect the DSD variations [39] and at the same time internal dynamics (shallow layer with the upper layers) at the hills tops contribute the number-controlled processes such as collision-coalescence, breakup and further leads to the generation of smaller drops. These processes are in dynamic equilibrium contributing to the fact that smaller drops have a uniform vertical profile at high-altitude region. The presence of smaller drop with a high concentration in lower RR could be associated with the BB features where BB events contribute to DSD at smaller rain rates [39]. The drops originate from the BB could have less liquid water content [Fig. 6] and may contribute the less rainfall just below the melting layer height, but undergoes the collision-coalescence process and affect the total rainfall near the surface, and thus a sudden increase in drop size is observed just below the median BB height.

5. Campaign periods over Huancayo

5.1. Synoptic conditions during the dry and wet spells

Figure 10a shows the daily rainfall data recorded during campaign periods between February 18 and March 14, 2019. It is observed that the campaign periods could be divided into dry and well spells and mostly rainfall took place between March 4 and March 10, 2019. On the 10 March 16.3 mm rainfall was recorded in 24 hours, followed by 7 March and February 25 2019, with 12.2 and 10 mm. The dry spells are characterized between the February 20 and 24 and between February 26 and March 3, where daily rainfall was less than 2 mm. Figure 10b shows the diurnal variation in the rainfall during the campaign periods and again reveals the afternoon and night-time have higher rainfall during the campaign periods. However, the specific humidity field (Fig. 12) for the period with rainfall (wet spells), that the humidity isolines are more elongated to the west (with a quasi-zonal axis), corresponding to the period with less rainfall. The above is an indication of a greater transport of moisture from the Amazon to the central Sierra in the case of days with rain. The analysis of the period between February 20 and 24, when it practically did not rain on the observatory, confirms what was seen in the previous case. Here the situation is similar to that of the period between February 27 and on March 3. At 700 hPa circulation is greatly weakened, which does not guarantee the entry of moisture from the Amazon, while at 200hPa the anticyclonic circulation has become very distorted. Also the trough on the ocean penetrates towards the north, locating its axis to the west of Peru, which blocks the flow of the east on the Peruvian territory. In this case, it is important to emphasize that this trough, even, has a long-wave and greater depth than in the previous case, in which the wave is shorter.

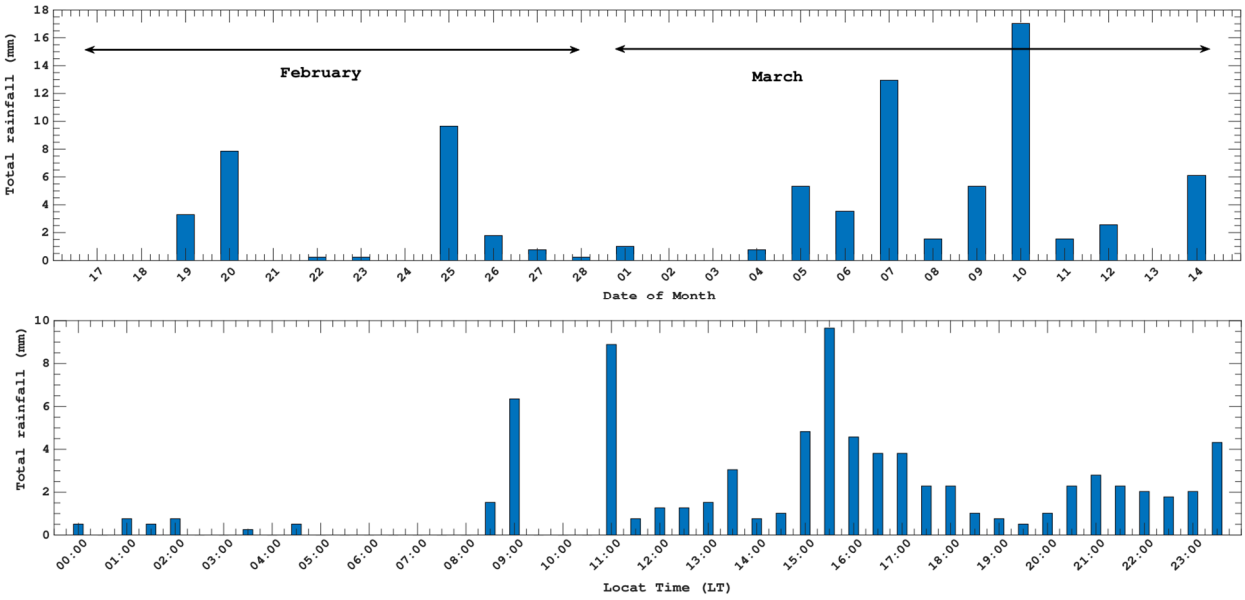

Figure 10. Precipitation (mm/24h) recorded at the Huancayo observatory between February 18 and 11 March 2019.

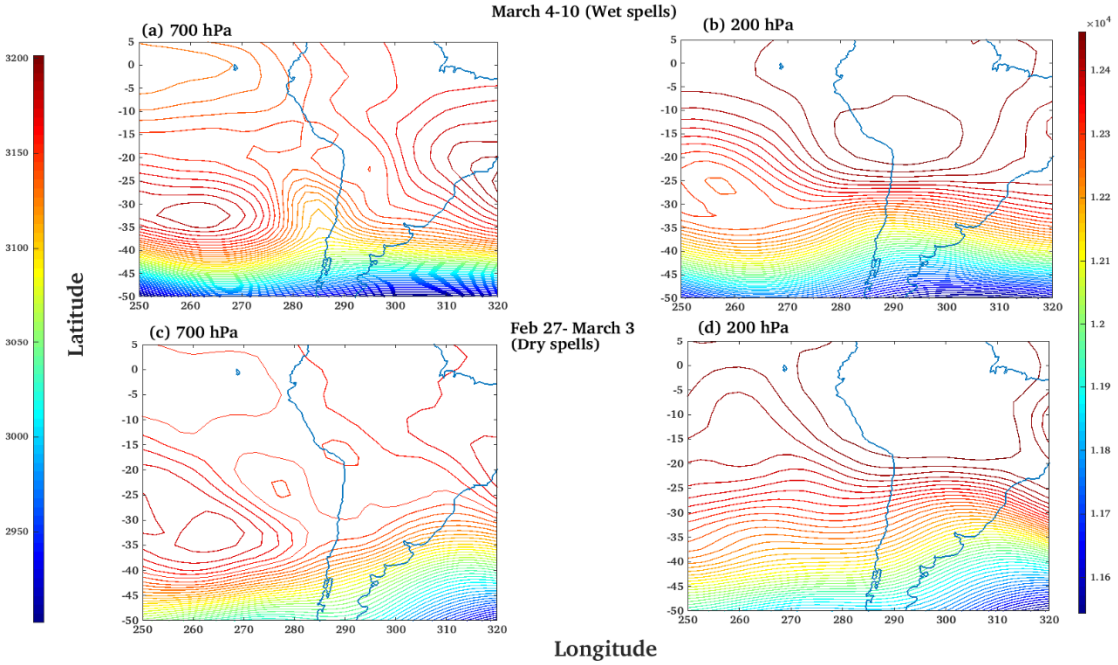

Figure 11. Average of geopotential height during wet and dry spells at 700 hPa and 200 hPa.

Figure 11 shows the synoptic behavior during dry and wet spells as mentioned earlier. Figure 11a shows the average geopotential height field at 700 hPa for the period between 4 and 10 March (wet spells) and observed that South Atlantic anticyclone ridge is well established and extends to the near Bolivia and the outskirts of the border between Brazil and Peru, which guarantees a humid airflow of the eastern region, from the Amazon to the central zone of Peru. Also, note that a good "trough" established in the vicinity of Pacific Ocean at the Peruvian coast. At the 200hPa (Figure 11b) the high pressures were established, with their center of circulation in the near the border between Peru, Bolivia and Chile, which guarantees a divergent flow of the eastern region over the central zone of Peru, which constitutes an important requirement for the occurrence of rainy days in this zone of the country, according to the studies carried out in this regard [2-3,9]. Another important element is that the trough over the ocean is located at South of the latitude of Peru in the form of a short wave, which allows anticyclonic circulation over the area of interest. A different features are observed in Fig. 11c;d corresponding to the period between 27 February and March 3 (dry spells). During the dry spells at 700 hPa the South Atlantic anticyclone ridge is moved towards the east, leaves a very weak flow between the Amazon and the central Sierra, so the supply of moisture to this region of the country would not be the same in the period analyzed above. Similarly, the "trough" on the ocean in the vicinity of the Peruvian coast is much weaker than in the previous case. For this period, as can be seen in Fig. 11a, the center of high pressure has moved to the northeast, what the predominant flow over Peru is confluent in the western region, which does not favor the occurrence of precipitation over the region.

Note in this case that the trough over the ocean penetrates more to the north. The analysis of the averaged moisture fields (Fig. 12) showed no significant differences between both periods, so can infer that the dynamics of flow over the region plays a fundamental role once the content of humidity on the area is sufficient for the generation of rainfall.

Table 4. Meteorological and VPPR statistics for the case studies. Upper-level winds are derived from ERA-Interim data for the grid cell closest to the VPPR at the event location and at the reanalysis hour closest to the middle of each event. Surface meteorological

variables were obtained from SPZO and a station collocated with the La Paz VPPR. Duration values are calculated using 3-h breaks and, therefore, represent parts of the event that may exist outside of the range of the VPPR image.

Date	Time	03/06	03/07	03/08	03/09	03/10	03/11
850-hPa wind speed (m/s)	00 UTC	8.7	6.8	14.3	11.5	15.5	3.9
	06 UTC	3.4	10.7	14.1	11.9	10.4	2.3
	12 UTC	4.5	15.2	14.5	11.0	11.6	2.1
	18 UTC	1.5	15.0	10.9	11.7	5.4	0.5
850-hPa wind direction ()	00 UTC	241	194	184	85	196	242
	06 UTC	250	191	86	188	192	231
	12 UTC	38	88	87	70	208	74
	18 UTC	211	184	185	184	236	78
500-hPa wind speed (m/s)	00 UTC	3.7	6.4	5.9	6.2	3.3	2.6
	06 UTC	2.1	6.2	9.2	7.4	5.8	6.8
	12 UTC	8.3	8.1	7.6	6.2	5.8	6.0
	18 UTC	9.5	7.5	6.7	5.6	3.6	2.6
500-hPa wind direction ()	00 UTC	256	76	66	187	78	36
	06 UTC	188	199	208	200	208	78
	12 UTC	220	84	204	197	210	108
	18 UTC	197	182	209	207	190	187

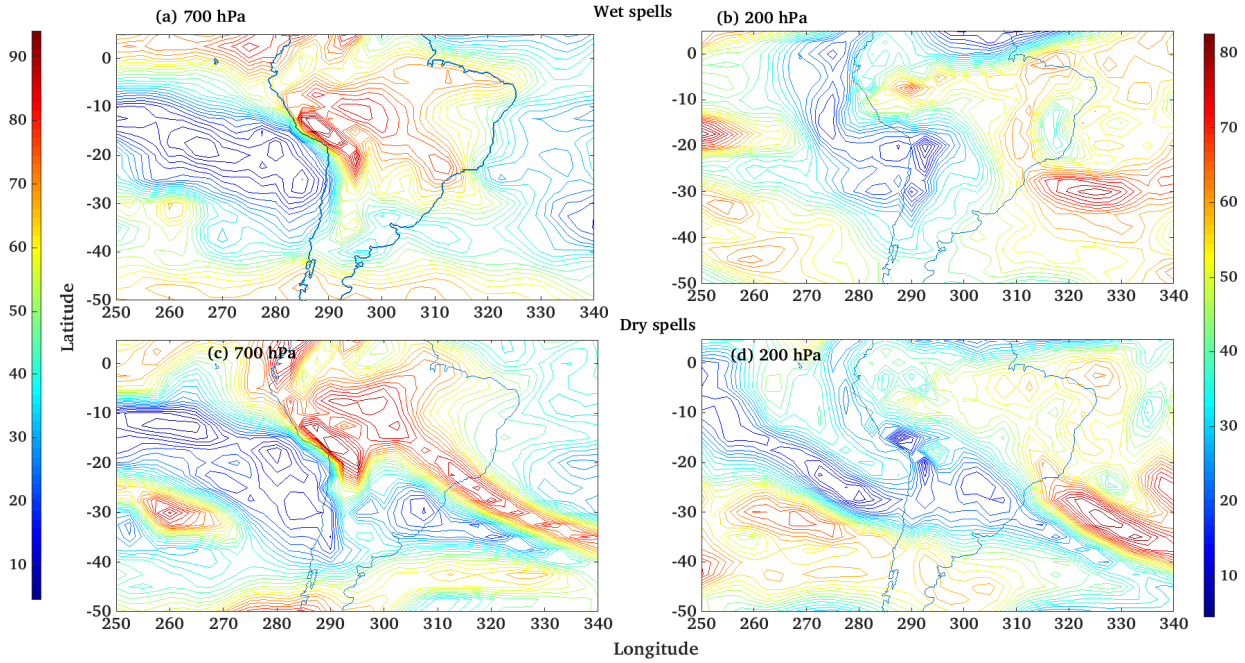

Figure 12. Humidity profiles for wet and dry spells at mid level pressure level (700 hPa) and upper level pressure level (200 hPa).

5.2. Vertical profiles of reflectivity and wind measurements during the rainy periods

Figure 13 shows the vertical profile of temperature collected during the wet spells in the early morning (07 LST) and afternoon (19 LST) along with dry and moist lapse rate and temperature profiles are nearer to moist lapse rate in the nighttime. We did not find any significant inversion mechanism during the rainy periods and all the profiles cross the 0°C only once, mostly lies between 5250 and 5550-m and nearly 150-200-m higher than the observed climatological BB (see Fig. 5). These results are consistent with the finding of the [79], where BB existed 253 m below the 0°C level because of the time taken by the frozen hydrometeors to melt with respect to ambient temperature. Figure 14 and 15 shows the vertical profile of Z_e and vertical velocity from the MIRA35 and BLTR respectively during wet spells. It is observed that most of the higher rainy days (wet spells) consist of the cloud systems with well defined BB structure rather than intense convection [46]; although few convective events are also observed [4] and discussed later. For example, the day with the highest rainfall (10 March, 16.8 mm) has a clear BB feature between 4:00 to 5:00 UTC. Intense convection is observed at the 23:40 UTC and lost for nearly 3 hours, and later followed by stratiform precipitation with BB features. Second row shows the accumulated rainfall for each day and 10th March has higher accumulated rainfall followed by 7th March, and could be related to higher convective rainfall with short-lived convective activity (Fig. 14). Table 4 provides details information about the dynamical behavior for each day (6 March to 11 March) at each 6-hour interval at different pressure levels using ECMWF data at 1^0 x 1^0 grid resolution.

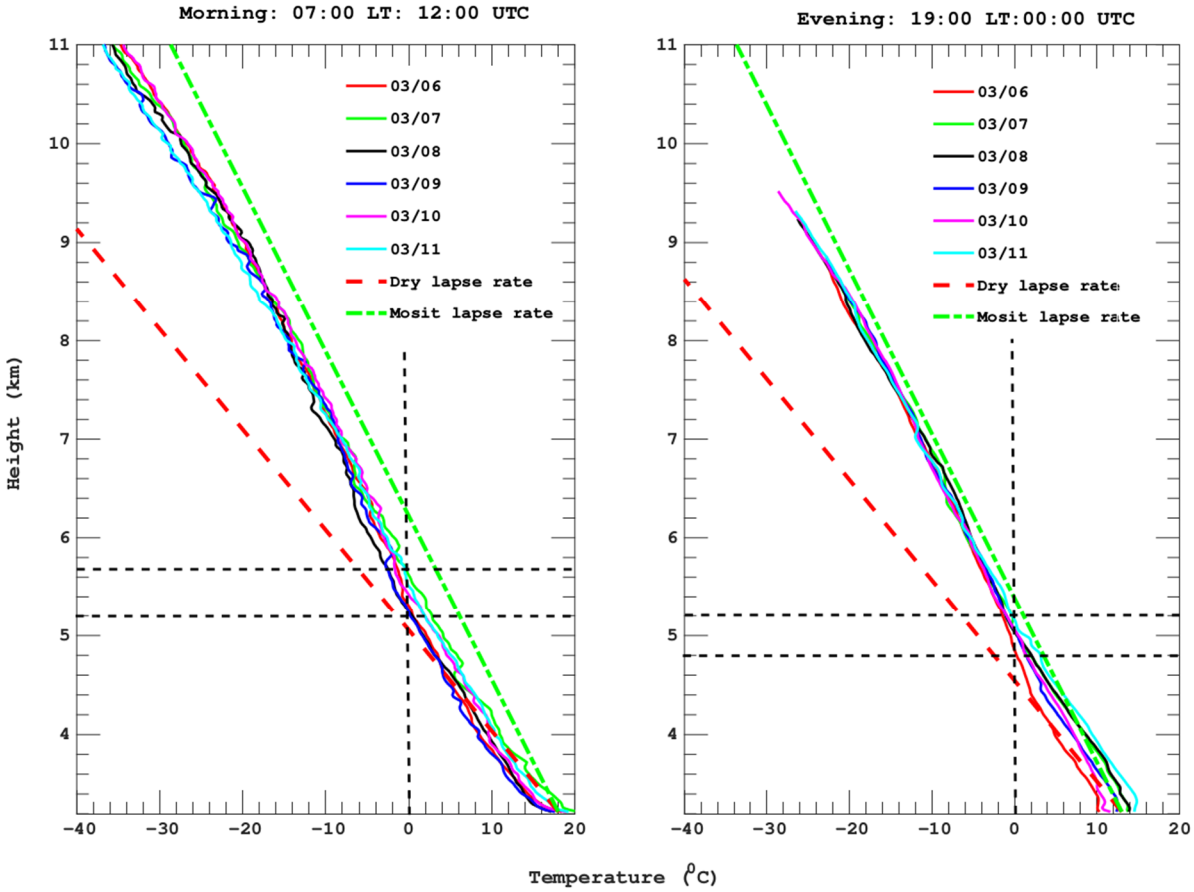

Figure 13. Vertical temperature profiles during rainy periods recorded by radiosonde launch on March 6 to March 11 at the site of the Huancayo VPPR. Representative moist- and dry-adiabatic lapse rates are indicated by the long- and short-dashed lines, respectively.

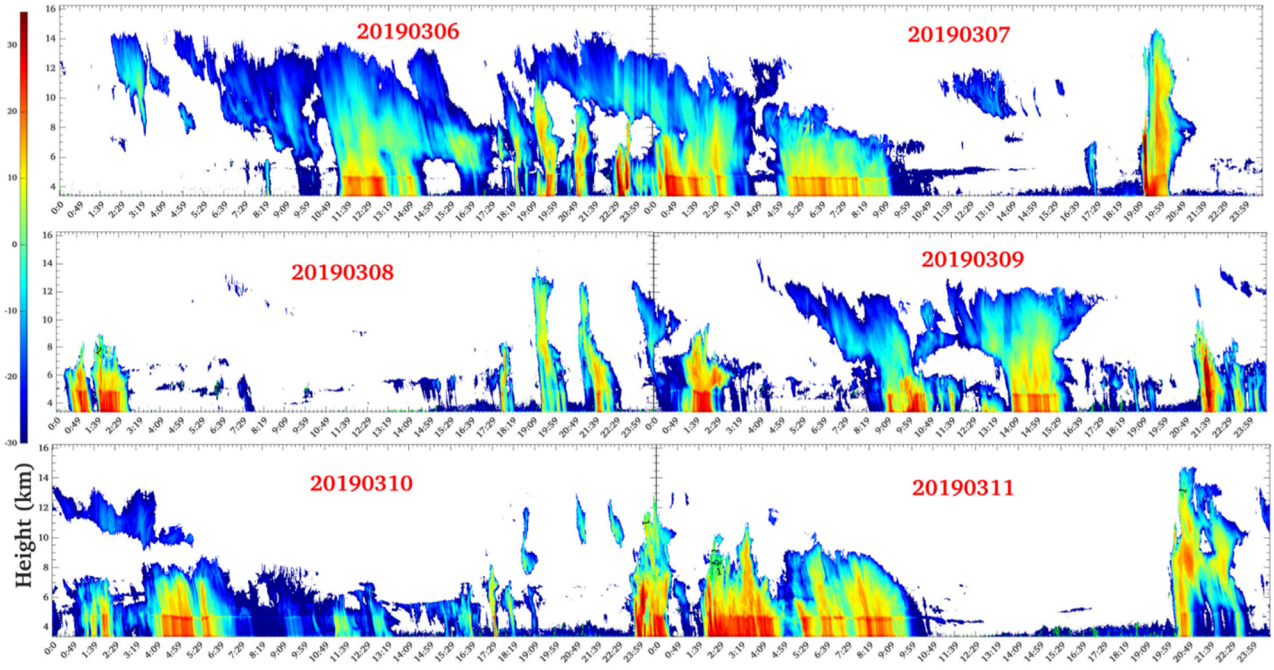

Figure 14. Vertical profile of radar reflectivity (Ze) during the wet spells (March 6 to March 11 2019) from VPPR.

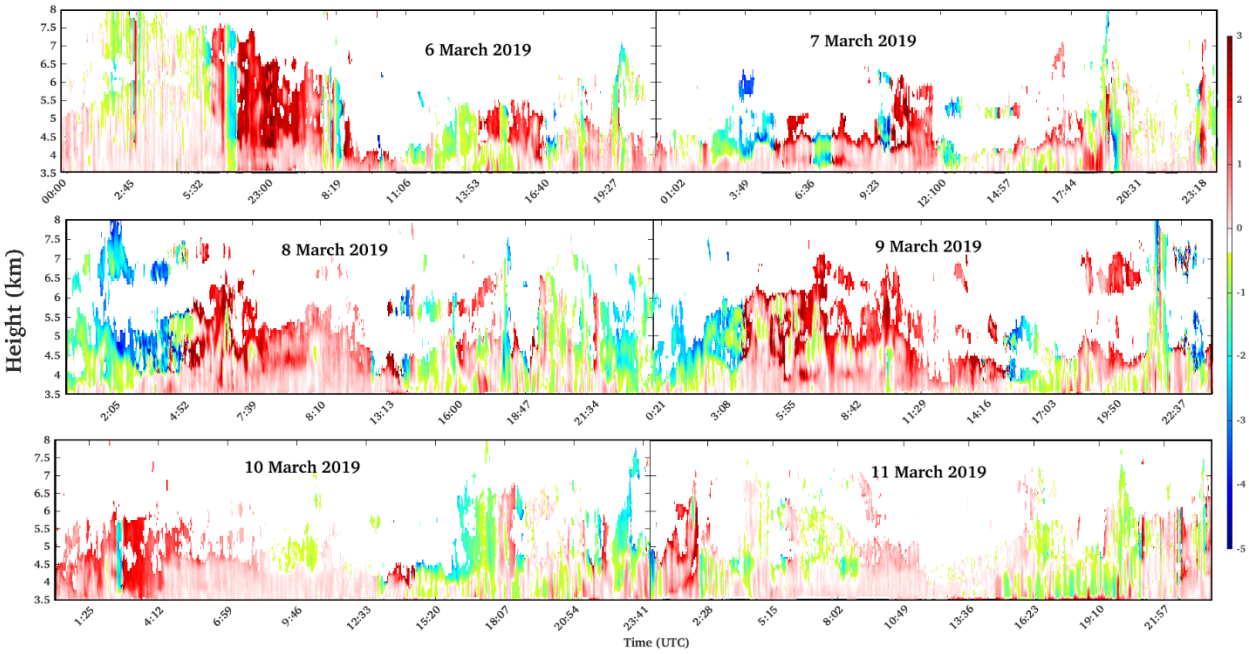

Figure 15. Vertical profile of vertical velocity during the wet spells (March 6 to March 11 2019) using BLTR data.

5.3. Convective and stratiform rainfall activity

It is well known that the rainfall and amount of the cloud fraction over the MB is modulated by the moisture convergence in the easterly and westerly flow [9,61] and triggers the convective activity [4,9]. At the same time, orographic features are also very important to produce rainfall over HYO, as orography could modulates the different wind at different pressure levels [7-8,35,60-61]. In summer

months, intense heating of Earth's surface, because of the large availability of solar energy, favors the development of convective clouds [80]. In a recent study, Flores et al. [9] showed that southern displacement of the South-east Pacific Subtropical Anticyclone up to latitudes higher than 35°S, weakening and south-eastern displacement of the BH-NL system and intrusion of westerly winds along the west side of the central Andes at upper and medium levels are important to generate the thunderstorms over HYO. For example at the meso-scale, convergence of two important fluxes from north-west and south-east side of Andes trigger the deep convection into the MB. The intrusion of the sea breeze from the Pacific Ocean along the west of the Andes and couples with upper and middle westerly winds and thermally induced moisture fluxes from SA-LLJ is the main moisture fluxes in these areas. However on the local scale previous hours conditional instability also simulate the thunderstorms. For example, SPSA generates the subsidence which causes the arid and stable conditions along northern Chile and southern Peru which extend over the inland over the western slope of the Andes [61]. The other important dynamical feature is BH and north-east low (NL) and main circulation over South America during the Austral summer [61].

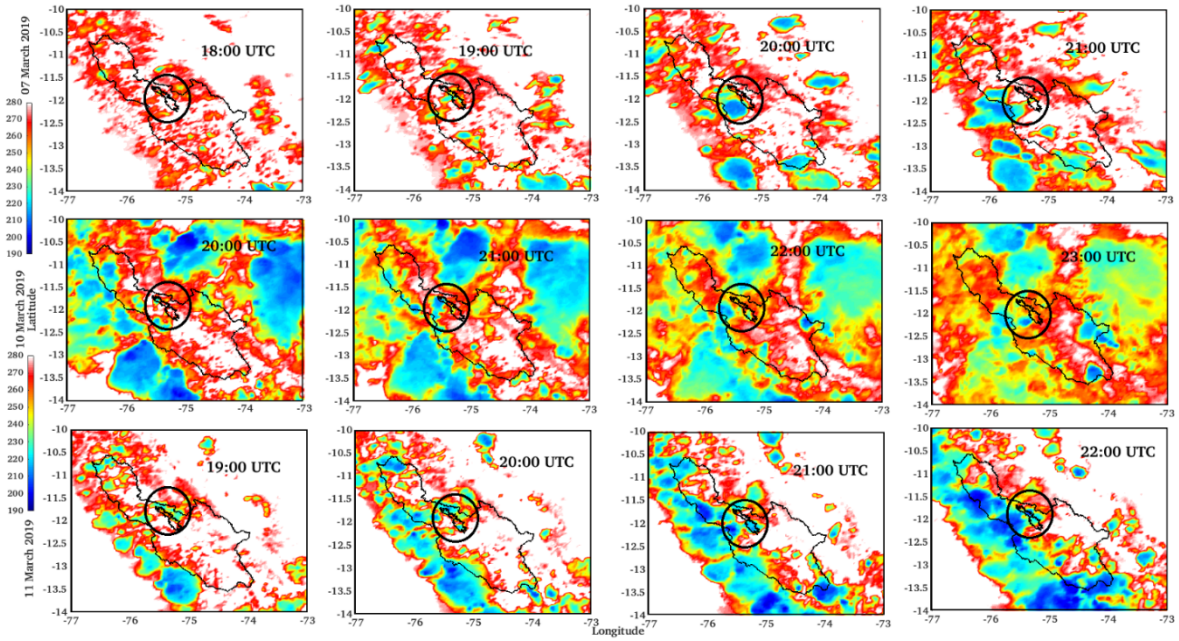

Figure 16. Images of the GOES infrared channel for the period of development in the area of the Mantaro river basin for convective rainfall events. The color bar indicates the brightness temperature. The UTC in hours is indicated for each image. The contour of the basin is shown with a continuous line, and inside, the outline of the valley is highlighted, approximately in the center of each square.

Based on the MIRA35 and BLTR data we identified the three convective and two stratiform precipitation events (CPEs and SPEs) and tabulated in table 5. We would like to investigate the evolution and dynamical behavior during the CPEs and SPEs of the cloud systems, from where they generate and reaches up to HYO. From the table, it is clear that CPEs have much higher accumulated rainfall compared to SPEs and documented in a recent study [4,9,46]. For example, the first CPE produces ~7.4 mm of accumulated surface rainfall within one hour (19:00 to 20:00 UTC on 7th March) whereas second CPE produces ~2.01 mm of rainfall within one and half hour of the convective activity. The SPEs show the different characteristics compared to CPEs and lost for many hours but produce less rainfall. For example, first SPE occurred on 7th March between 00:00 UTC to 10:00 UTC and produces 3.55 mm of accumulated rainfall with median BB height occurs at ~4.56 km, whereas other SPE lost for nearly 8 hours (00:00 UTC to 07:30 UTC) and contribute 1.01 mm of accumulated rainfall with BB lies nearly 4.70 km. Both the SPEs mostly occur in the afternoon and nighttime and consistent with the past findings of the stratiform precipitation over different tropical locations over tropical Andes mountain [46].

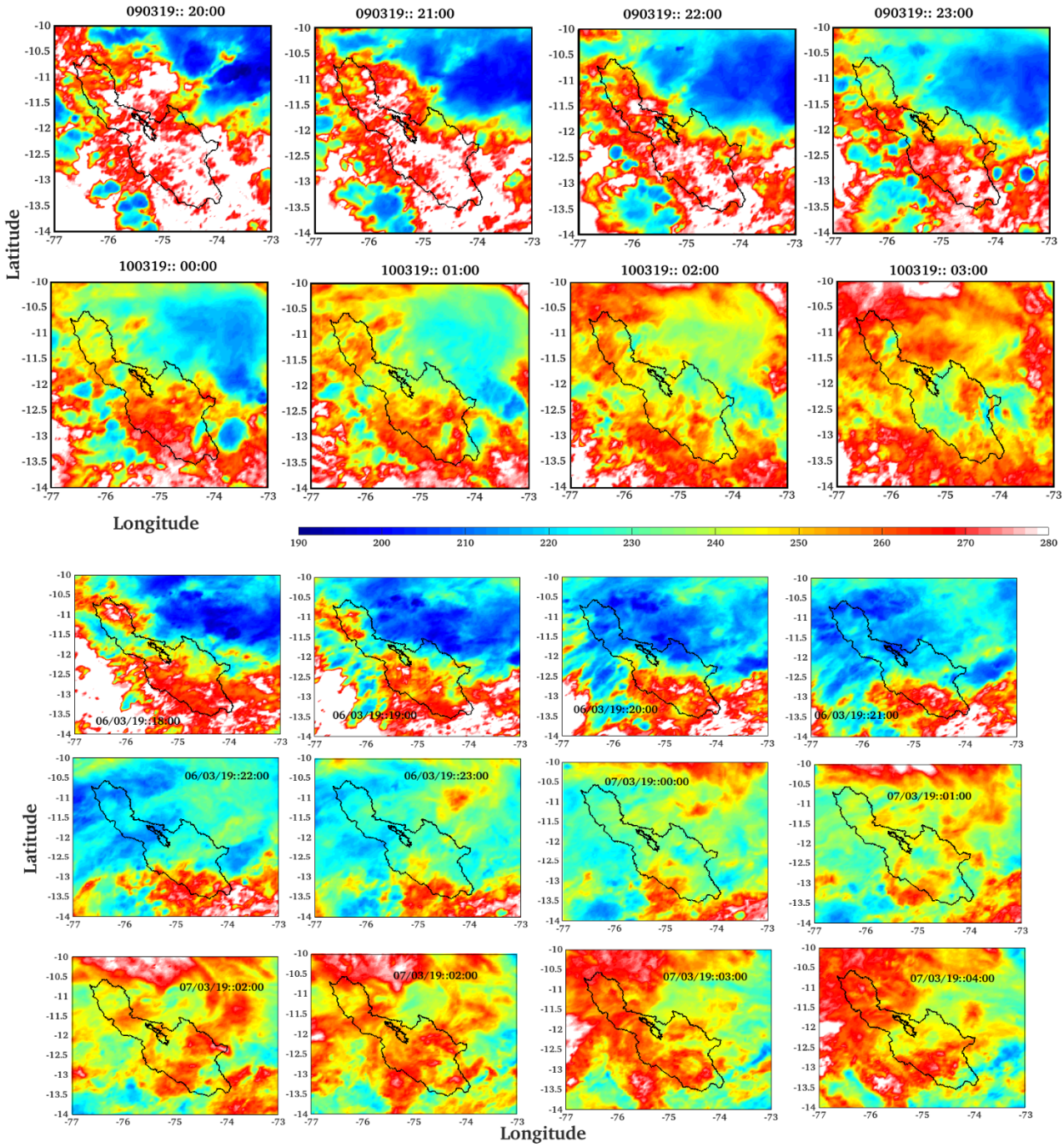

Figure 17. Images of the GOES infrared channel for the period of development in the area of the Mantaro river basin for stratiform rainfall events. The color bar indicates the brightness temperature. The UTC in hours is indicated for each image. The contour of the basin is shown with a continuous line, and inside, the outline of the valley is highlighted, approximately in the center of each square.

To investigate the evolution of the CPEs and SPEs, the BT from GOES are shown. Figure 16 shows time series for the BT for all the CPEs and SPEs for 7th, 10th and 11th March during the campaign periods. It is observed that convective activity developed mostly at the south-west of the HYO and moves towards the north-east (Fig. 16) and generate the copious rainfall [4,9]. For example, the first CPE generated at the west of the HYO at ~8:30 UTC and moves towards the north east and produces the copious amount of surface rainfall. A simultaneous convective activity is also observed at the east of the HYO but not able to reach to HYO [4,9]. For the second and third CPEs, it is again confirmed

that convective activity mostly develops at the west of the HYO and then moves at the northeast. However, the SPEs show the different features/characteristics and both the SPEs generated at the east of the MB (in the Amazon forest and low lands area of the SA) and reaches HYO (Fig. 17) which is known as to consists of the largest squall lines and large number of meso-scale convective systems [13-14,35,60,81] and moves towards the east of the Andes mountain under the influence of SA-LLJ [9,15-16,61] and surface winds [35].

Figure 18 shows the wind vectors and reduced sea level pressure for the 7th, 10th and 11th March (a,b and c respectively) using the GFS reanalysis data (resolution: 1°). On the 7th March, an SPSA is generated and centered near 40°S and moves at the northern SA continent. The lower/less value of atmospheric pressure level at the southern SA (990-995 hPa) and along the coastal latitude of MB (1000 to 1010 hPa) could diminish the subsidence effect over the coast pacific and favors the intrusion of the sea-breeze [9]. On the 10th March lower/less precipitation is observed at the north-west of SA continent (995-1000 hPa) and inland over the eastern of the HYO, whereas for the whole day along the coastal latitude of SA diminishes the subsidence effect over the coast pacific and favors the intrusion of the sea-breeze. The 11th March also shows the similar features and an area of low pressure area is observed at the west coastal latitude of HYO. These low-pressure regimes at the coastal area produce rainfall activity over HYO [2-4,9]. Figure 19 shows the wind-stream lines at 18:00 UTC for the three mentioned days at lower, mid and upper pressure levels. At mid-level pressure (700 hPa) the wind circulations show the different characteristics for the three CPEs. On the 7th March 2019 (Fig. 19a), along the east side of the Andes, a well-defined north-easterly circulation was observed along that follows the SALLJ at 850 and 950 hPa. These north-easterly circulations could favor the intrusion of moisture from the Amazon basin to the central Andes. In contrast, on the 10th March (Fig. 19b) the easterly circulations are restricted to low latitudes (around 15°S), probably due to the disturbance produced by two anticyclone circulations centered at 20°S, 50°W and 40°S, 58°W, respectively. The last anticyclone was also observed at 850 and 950 hPa and is probably associated with the south-west displacement of the South-Atlantic high-pressure system (Fig. 19b), which generate south-easterly circulations along the east side of the Andes that could disfavor the intrusion of moisture from the Amazon basin to the central Andes. On the 11th March, the north-easterly circulations are partially re-established at 700 hPa, but they are less observed in the 850 and 950 hPa, where the presence of the South-Atlantic high pressure system is still near the south-west coast of Brazil (Fig. 19c). Along the west side of the Andes, at low-level pressures (850 and 950 hPa) a westerly circulation was observed which could favor the intrusion of moisture from the sea breeze and mountain valley circulations inside the Andes around the MB (Fig. 19c). These westerly moisture fluxes that intrude inside the high lands of the Mantaro valley can be observed in the band of cloudiness (Fig. 16;17).

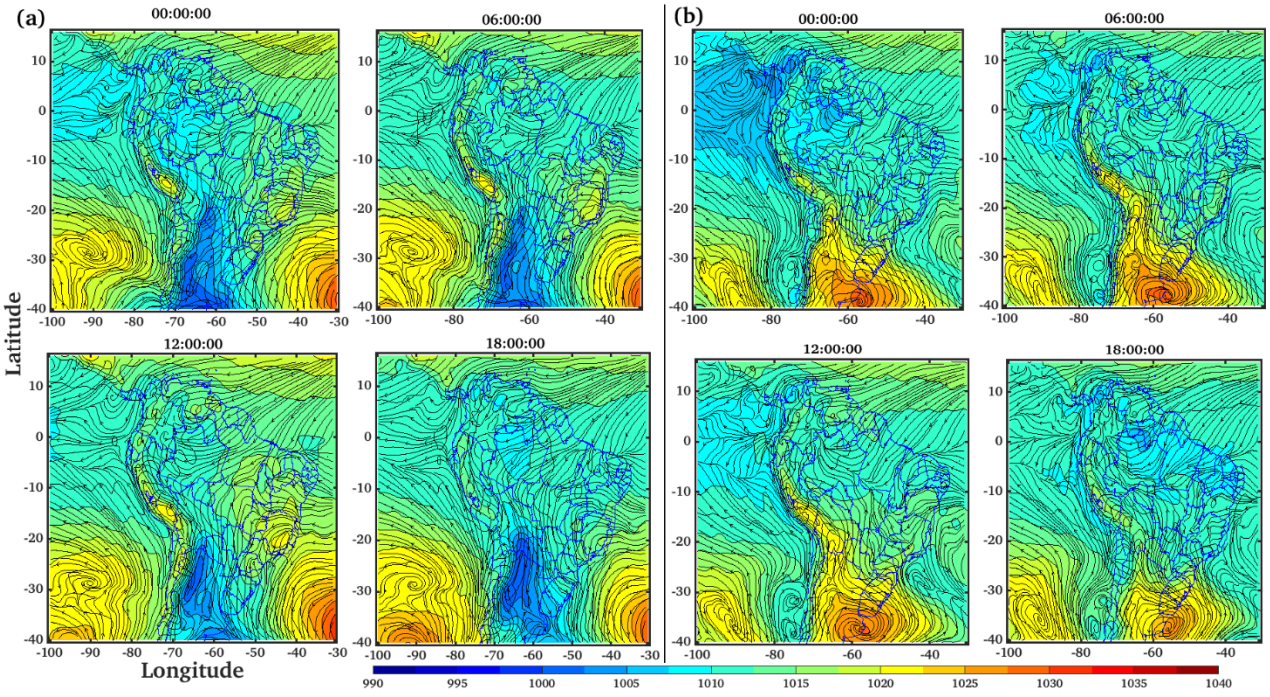

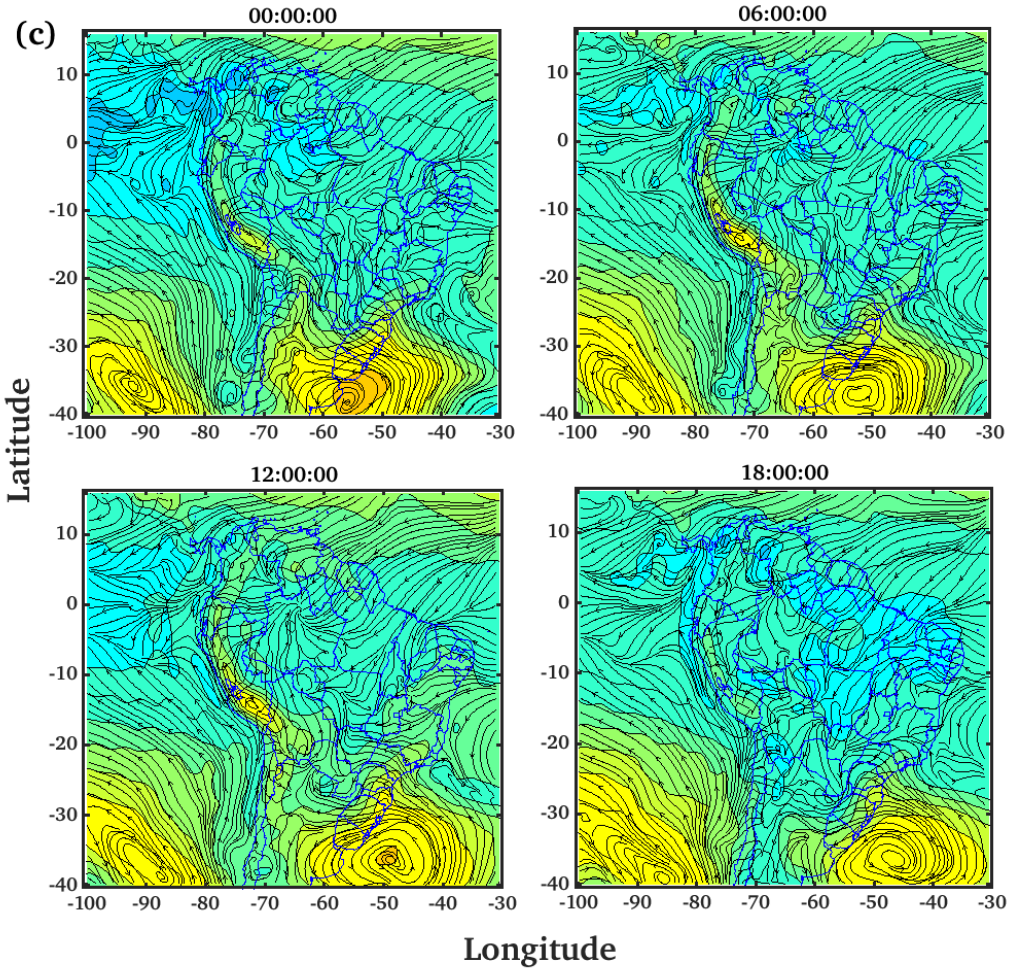

Figure 18. Wind streamlines and reduced pressure to mean sea level (hPa). Cold colors indicate lower values and warm colors higher values. All composites data were obtained for the convective events at 1800 UTC from the GFS reanalysis data (resolution: 1°).

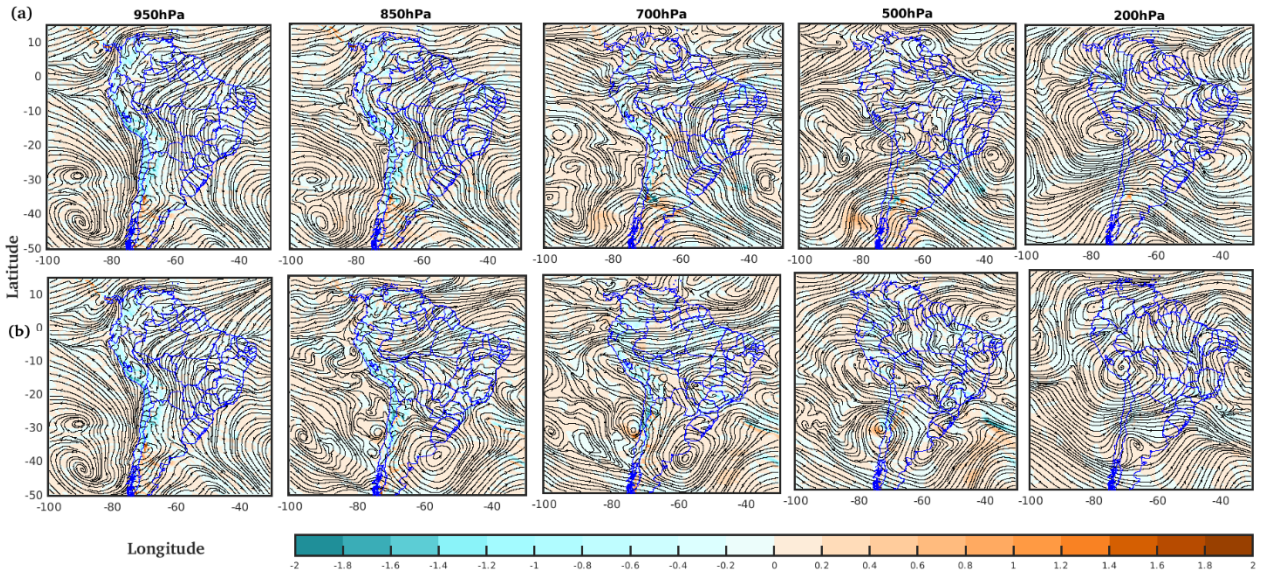

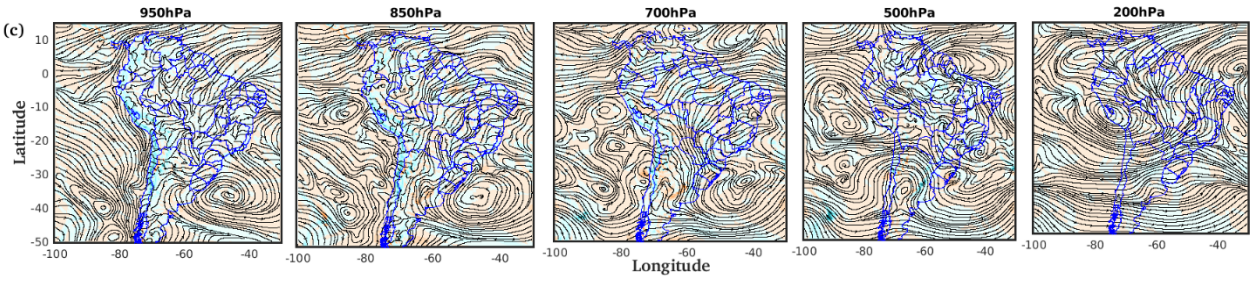

Figure 19. Wind streamlines (m s^{-1}) and vertical velocities (Pa s^{-1}) at high levels (700 hPa) at 18 UTC for three dates. Positive (negative) values indicate downdraft (updraft) winds. All composites data were obtained for the three convective events at 1800 UTC from the GFS reanalysis data (resolution: 1°).

The characteristics of the CPEs depend on both the static stability of the environment, wind speed and wind direction shear [82]. Sounding results between 06-11 March at 07 and 19 LST are shown in Fig. 20 and at 13 LST in Fig. 21. For all the rainy days, a stable atmosphere is observed at 07 LST that creates an air potential temperature gradient (θ) directed towards the surface with values between 315 K and 320 near the surface. For 07, 08 and 10th March, negative gradients of the equivalent potential temperature (θe) were observed at 07 LST, which indicates a slightly conditionally unstable layer in the first 4 km, probably caused by the presence of high moisture content in these days with surface value close to 340 K. In contrast, at 13 LST a high unstable condition was observed, with higher negative gradients in 07, 10 and 11 March. However, the release of conditional instability, which occurs when θe is almost equal to θe* (saturation equivalent potential temperature) near the surface, happened on 07 March at 1500 m, on 08 March at 3000 m and on 09 March at 2500 m. The key factor in producing a nonzero convective available potential energy (CAPE; Fig. 22) in these days, is the higher θe (350 K) near the surface. Probably, the higher θe near the surface is mainly produced by a higher mixing ratio near the surface. This behavior is maintained at 19 LST on 07 and 10 March with significant negative gradients in θe near the surface. Significant vertical wind speed and wind direction shear were observed on 07 and 10 March (Fig. 23), which contributes to increasing the longevity of convective processes. The super-cell structure in thunderstorm is promoted by strong environmental shear, which leads to strong mid-level vorticity on the storm

flanks. The negative dynamic pressure perturbations in these vorticities lead to vertical acceleration and continual regeneration of the updrafts on the two flanks of the storm.

Table 5. Time of occurrences, accumulated rainfall and bright band height during the convective and stratiform rainfall events during the campaign periods.

Convective activity			
Date	**Time**	**Total amount of rainfall (mm)**	**Median BB height**
07 / 03 /2019	19:00 – 20:00 UTC ,14:00-15:00 LT	7.3660	No
10 /03 /2019	23:00 – 0:30 UTC, 18:00 LT-19:30 LT	2.0320	No
11 /03 /2019	19:00 – 23:30 UTC, 14:00-18:30 LT	Nil	No
Stratiform rainfall activity			
07/03/2019	00:00 –10:00 UTC	3.5560	4.56 km
10/03/2019	00:00 –07:30 UTC	1.0160	4.70 km

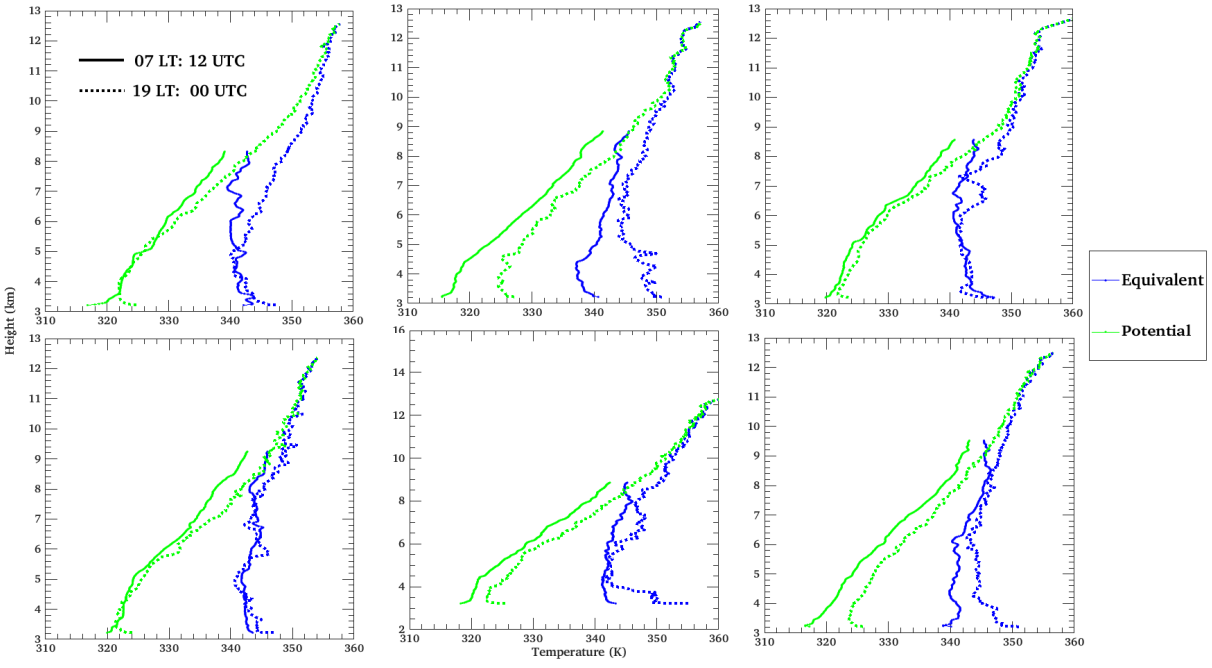

Figure 20. Vertical profile of equivalent potential and potential temperature during the rainy periods (6th March to 11th March 2019).

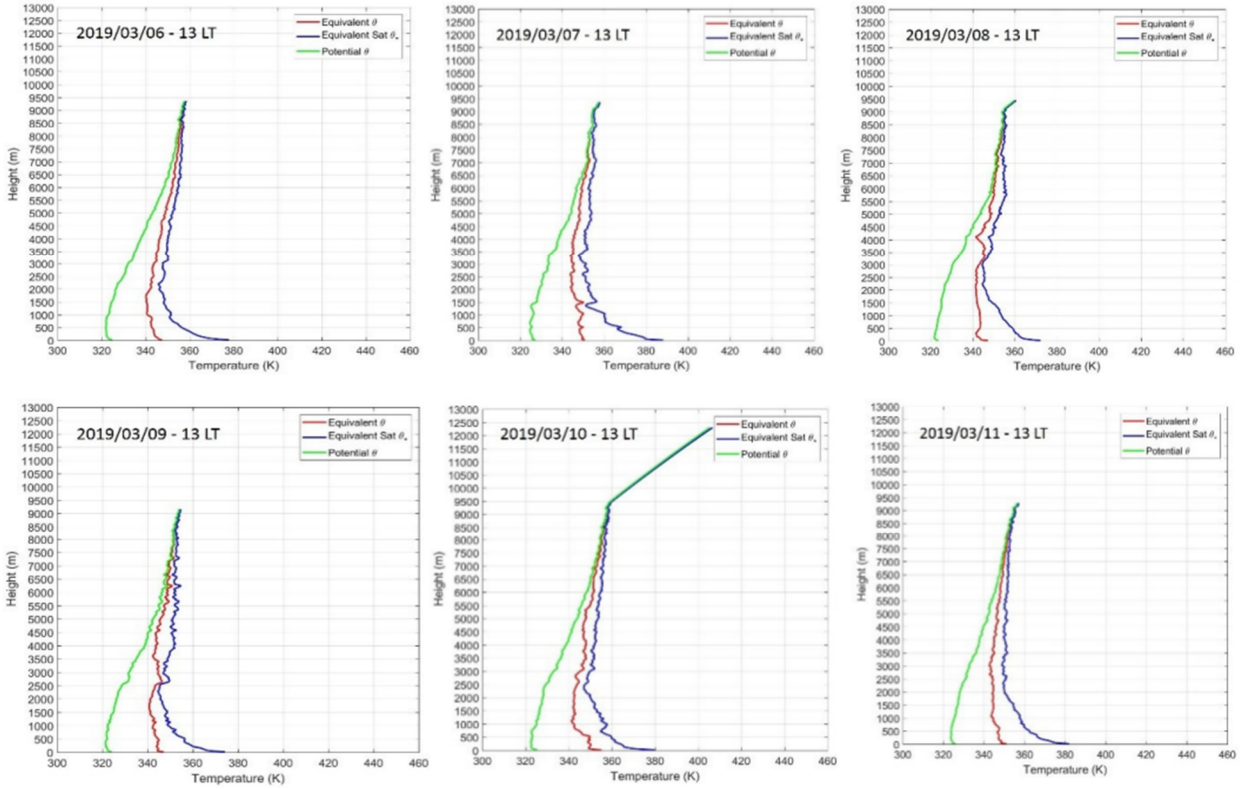

Figure 21. Equivalent Potential temperature, Saturation Equivalent Potential Temperature and Potential Temperature calculated from the radiosonde data for 06-11 March at 13 LST.

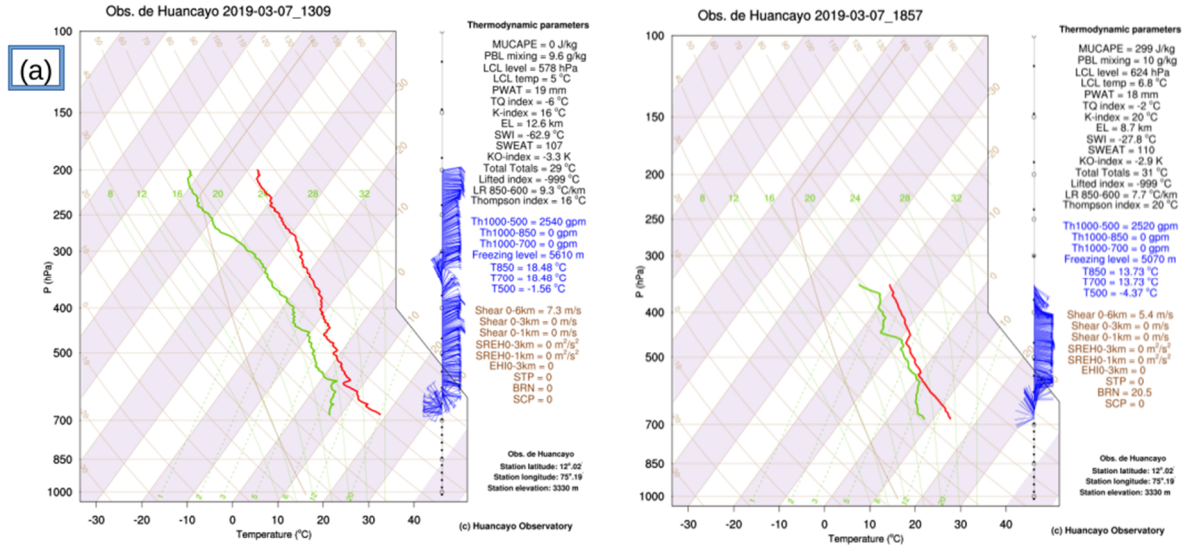

665

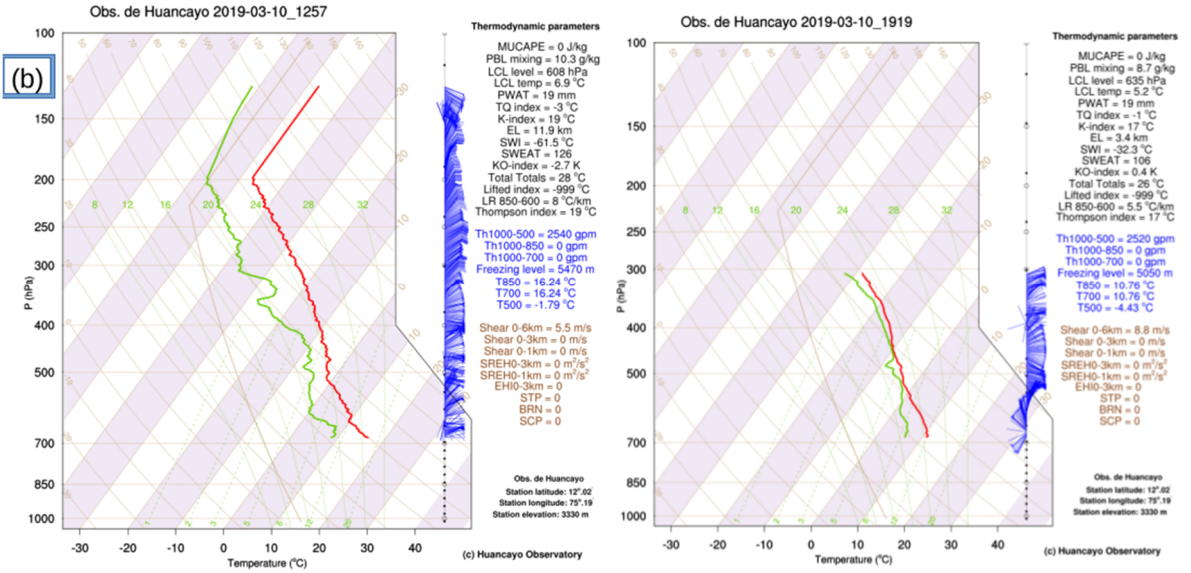

666

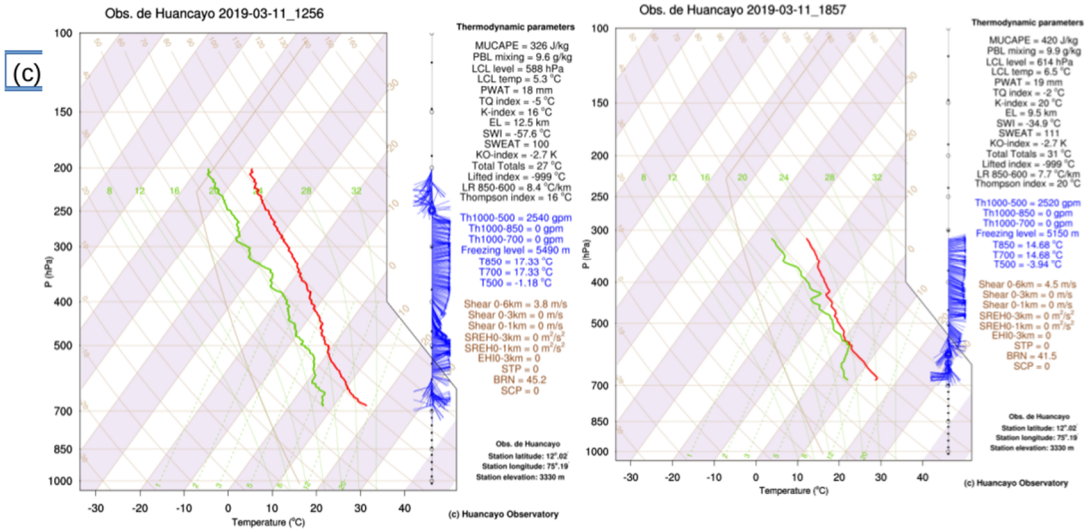

667

668 **Figure 22.** Skew-T diagram for the wet spells (6th March to 11th March 2019) using the
669 radiosone observations.

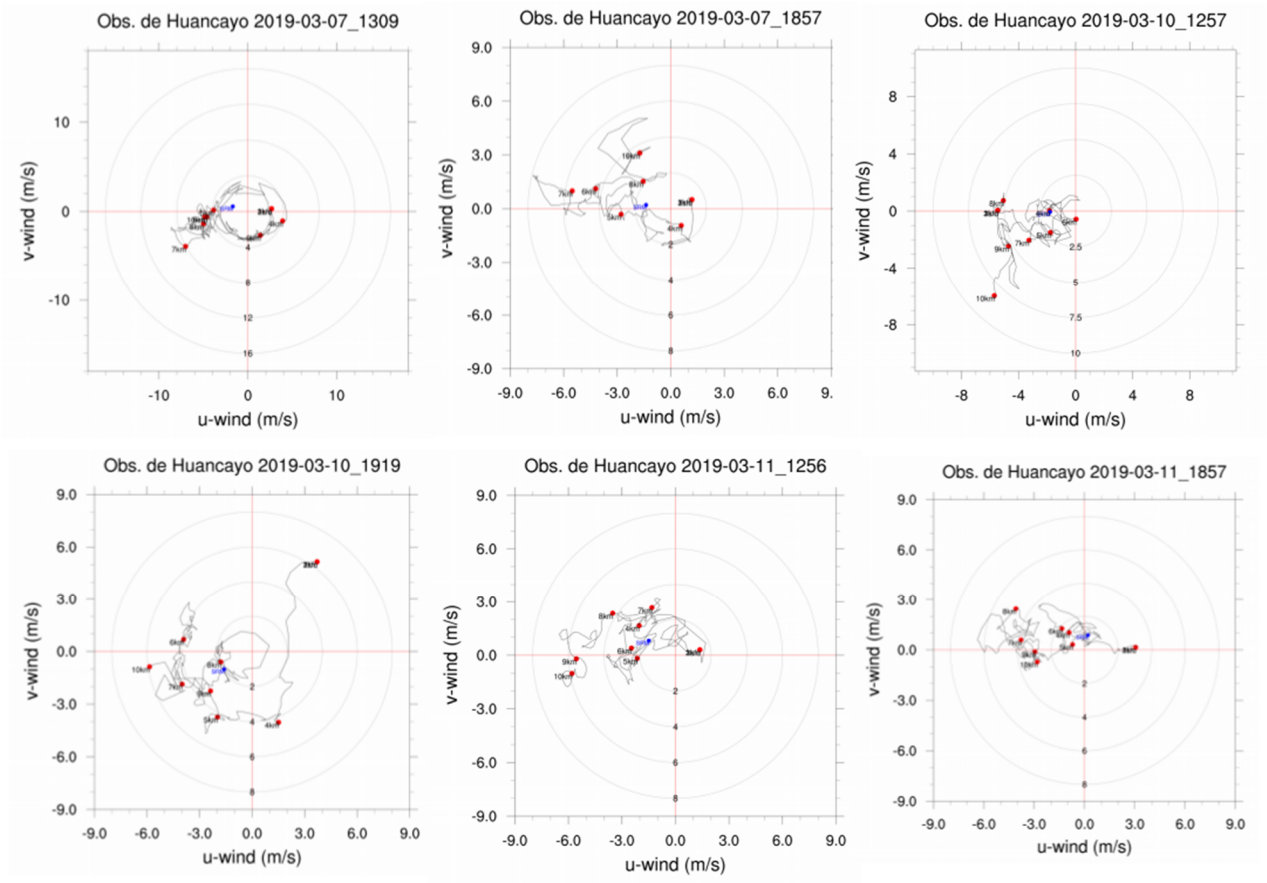

670

671 **Figure 23.** Wind direction and shear observed for the campaign periodsduring wet spells
672 (6th March to 11 March 2019).

673 **6. Summary, conclusions and limitations**

674 The present study presents the climatological rainfall characteristics including diurnal variation,
675 BB characteristics, and VSR characteristics of the rainfall. Also, in-situ measurement shows the
676 evolution/characteristics of the convective and stratiform precipitation and dynamics of the rainfall
677 patterns during wet and dry spells over the HYO. HYO is located at the west of the Amazon basin,
678 which is primary moisture source for the central Andes [45,57,83] and partially explained the
679 variability in the rainfall observed over HYO. A bimodal pattern in the rainfall is observed and
680 maximum RR BB height occurred in afternoon and nighttime and associated with a deep, well-mixed
681 planetary boundary layer following daytime surface heating [45-47]. In-situ observations show the
682 wet spells have short lived convective cells and long-lived stratiform precipitation with a layered
683 well structure of well defined BB with weaker vertical air motion [46,84-85]. The dominance of the
684 stratiform precipitation over the tropical Andes was previously observed in radar studies [13,47,59]
685 and nighttime higher precipitation over the tropical Andes associated with Amazon basin in MCS
686 structure [13,15-16,35,60,86]. These lowland MCSs could reach at a higher Andes altitude because of
687 daytime heating in upslope flow and by the convergence of downslope flow, which develops from
688 rapidly cooling high terrain [13,15,35]. For example, daytime heating over the higher Andes altitude
689 induces the upslope valley breeze and sufficient moisture flux initiate the precipitation [13,15-16]. At
690 the same time evaporating cold downslope flow converge with the north-easterly Amazon moisture
691 flux and induce the precipitation over the tropical Andes [13,15,16,35,59]. Whenever there are no

clouds in the overnight, the radiative cooling induced the downslope flow interacts with the Amazonian moisture and induces the nighttime precipitation peak in the valleys [13,58]. Chavez and Takahashi [86] showed that SALLJ along the eastern slopes of the Andes can also be impeded by weaker nighttime upslope flows, feeding organized convection at lower elevations. Orographic precipitation also increases the local precipitation, which mainly occurs due to stratiform precipitation associated with seeder–feeder mechanism [45-47]. BB height is higher at afternoon and night-time and [46-47,87-88] and increases due to long-duration stratiform precipitation [46]. Perry et al. [47] showed that BB heights greater than 5 km over the nearby tropical Andes represent the occasional rainfall occur in alpine zones such as on the Nevado Chacaltaya. The higher differences in VSR in the mixed phase regimes (6-9 km) are related to the ice microphysics processes [70]. For example, the hydrometeors which are lifted in upper troposphere in the early phase of evolution started their downward under weaker velocity and increase in size due to cloud ice microphysics. Houze [89] showed that convective and stratiform precipitation consists of different microphysical processes and they significantly impact on the latent heat profiles and DSD parameters. For example, in well matured stratiform cloud, falling ice particles from cloud top grow by deposition of vapor to a moderately large size, then within about 2.5 km of freezing level, aggregation and rimming process occurs to form irregularly shaped large snowflakes which then melt at 0°C isotherm level and produce BB signatures [71-74]. Based on the present study the major finding of the presents are mentioned below:

1. A bimodal patterns are observed in precipitation with local maxima in the precipitation during after-noon and overnight and shows the higher afternoon and nighttime RR and accumulated rainfall. Both JJAS and SON months show the same features and mean RR is slightly higher during pre monsoon seasons compared to monsoon seasons. However the highest accumulated rainfall observed between 12:00 to 14:00 UTC during JJAS months, whereas during SON the highest accumulated observed during 19:00 UTC to 21:00 UTC.

2. The BB clearly shows the diurnal variation, and, afternoon and nighttime BB height are higher compared to early morning BB for both the seasons and consistent with the diurnal cycle of surface temperature in the tropical Andes [46]. Also, the median BB height occurs around ~4.7 km altitude. The vertical profiles, which consist of the BB have higher Z_e above the freezing height and revels the melting of ice could produce higher rainfall. More than 20% BB height is higher than 5 km altitude and has important implications on the climate of the Andes.

3. The vertical structure of Z_e and DSD information are important for predicting the correct estimation of rain information. Also, the vertical evolution of DSD is important to investigate and characterize the rainfall information. The information presented here is important consequences in space based radar retrieval of precipitation. The average Z_e profiles have show the gradient near the freezing height due to melting layer and for the higher near surface RR, Z_e decreases sharply above the freezing height and consistent with the TRMM and GPM observations. RR and LWC show the differences in vertical variation below and above the 6 km altitude. The DSD variation shows the higher concentration of higher drop size for higher RR below the freezing height and even higher for higher RR and shows the effect of BB height and discussed in the txt. The DSD could be assumed/responsible for VSR behavior. Convective rain is found to have a larger drop size at ground level than that of stratiform rain.

4. The rainfall patterns/characteristics during campaign data reveal the convective organization with higher precipitation, however stratiform precipitation is more common and exist for the longer periods. Most of the convective activity generated at the west of the Andes and moves north-west to reach the HYO and produces the copious rainfall [4,9]. However the stratiform precipitation at HYO comes from the east of the Andes and generated over Amazon and moves at the eastwards. The sounding results showed that CPEs depend on both the static stability of the environment, wind speed and wind direction shear. Higher θe (350 K) near the surface produces the higher CAPE values during convective events. Strong environmental shear leads the strong mid level vorticity to create the organized thunderstorms, and negative dynamic pressure perturbations in these vorticities lead to vertical acceleration and continual regeneration of the updrafts on the two flanks of the storm.

744 5. Dry and wet spells over the HYO consist of different dynamical behaviors at different pressure
745 levels. For example the circulation at low levels guarantee the transport of moisture from the Amazon
746 to the central Sierra of Peru, while the anticyclonic circulation at high levels guarantees the
747 divergence at high pressure levels and, favours, the development convective on the region. While,
748 during dry spells the circulation at low levels are very weak on the west of Brazil and Peru, limits the
749 transport of moisture to the central Sierra, while the circulation at high levels does not favor rain
750 processes. These cases confirm the importance of transportation humidity from the Amazon towards
751 the Peruvian Sierra and the presence of the anticyclonic circulation at high levels, centered in the
752 vicinity of Bolivia and southeastern Peru.
753 However, more investigations are required to disentangle the relationship between convection
754 triggering and its development into organized precipitation and how these organized precipitations
755 affect the tropical Andes weather and climate. The present study improves the understanding of
756 characteristics of rainfall using the ground based observations and in-situ observations, however
757 several uncertainty induces the errors in the outcomes. For example, a VPPR can only
758 observe/measure the cloud systems/hydrometeors which passing over it and could miss the intense
759 and other part of the cloud systems. Other issue is the algorithm used in the retrievals of
760 microphysical variables such as radar reflectivity and DSD variations. Peters et al. [26] explained that
761 the negative slope at higher RR is expected as the due could be because of the errors introduced by
762 overcompensation of the rain attenuation at high rain rate as mentioned in Das et al. [36] and also
763 observed in higher Z_e and RR profiles. However the positive slope in the LWC shows the correct
764 estimation and errors are very less in this RR range due to rain attenuation. The possible regions
765 behind such kind of behavior are the shift of the DSD peak and DSD peak toward smaller drops with
766 increasing height. The lowest class of RR generally associated with the drizzle (with Z_e<0 dBZ, Houze
767 [89] and related with the lower shallow clouds and with less fall velocity and associated with the
768 smaller drops [26,76]. At the same time, evaporation also plays a significant at very low rain rates
769 and lower height and alters the DSD and affect the small drops concentration and lead to the positive
770 gradient in LWC and RR profiles.
771 **Acknowledgement** Present study comes under the project "MAGNET-IGP: Strengthening the research line
772 in physics and microphysics of the atmosphere (Agreement No 010-2017-FONDECYT)". I would like to thanks
773 the CONCYTEC, Peru, for financial support and Inter-American Institute for Cooperation on Agriculture (IICA)
774 for administrative support. Two anonymous reviewers helped to clarify multiple aspects of the manuscript.

References

[1] Seto, S., Iguchi, T., Oki, T., 2013. The basic performance of a precipitation retrieval algorithm for the Global Precipitation Measurement mission's single/dual-frequency radar measurements, IEEE Trans. Geosci. Remote Sens., 51, 5239–5251.

[2] Moya-Álvarez, A., Gálvez, J., Holguín, A., Estevan, R., Kumar, S., Villalobos, E., Martínez-Castro, D. and Silva, Y., 2018. Extreme Rainfall Forecast with the WRF-ARW Model in the Central Andes of Peru. Atmosphere, 9(9), p.362.

[3] Moya-Álvarez, A.S., Martínez-Castro, D., Kumar, S. et al. 2019. Theor Appl Climatol. https://doi.org/10.1007/s00704-019-02782-3

[4] Martínez-Castro D, Kumar S, Flores Rojas JL, Moya-Álvarez A, Valdivia-Prado JM, Villalobos-Puma E, Castillo-Velarde CD, Silva-Vidal Y. The Impact of Microphysics Parameterization in the Simulation of Two Convective Rainfall Events over the Central Andes of Peru Using WRF-ARW. Atmosphere. 2019 Aug;10(8):442.

[5] Lin YL. 2003. The dynamics of orographic precipitation,Preprints of The Harold D. Orville Symposium, 26 April 2003. Institute forAtmospheric Sciences: Rapid City, SD, 68 – 89.

[6] Kirshbaum DJ, Durran DR. 2004. Factors governing cellular convection in orographic precipitation.Journal of the Atmospheric Sciences61: 682 – 698.

[7] Junquas, C., Li, L., Vera, C.S., Le Treut, H., Takahashi, K., 2016. Influence of South America orography on summertime precipitation in Southeastern South America. Clim. Dyn., Doi: 10.1007/ s00382-015-2814-8

[8] Junquas, C., Takahashi, K., Condom, T., Espinoza, J.C., Chavez, S., Sicart, J.E., Lebel, T., 2018. Understanding the influence of orography on the precipitation diurnal cycle and the associated atmospheric processes in the central Andes. Clim. Dyn., DOI 10.1007/s00382- 017-858-8

[9] Rojas, J.L.F., Alvarez, A.S.M., Kumar, S., Castro, D.M., Puma, E.V. and Vidal, F.Y.S., 2019. Analysis of Possible Triggering Mechanisms of Severe Thunderstorms in the Tropical Central Andes of Peru, Mantaro Valley. *Atmosphere*, *10*(6), p.301

[10] Silva, Y., Takahashi, K., Cruz, N., Trasmonte, G., Mosquera, K., Nickl, E., Chavez, R., Segura, B. and Lagos, P., 2006, April. Variability and climate change in the Mantaro river basin, Central Peruvian Andes. In *International Conference on Southern Hemisphere Meteorology and Oceanography (ICSHMO)* (Vol. 8, pp. 407-419).

[11] Giovannettone, J. P., and A. P. Barros, 2009: Probing regional orographic controls of precipitation and cloudiness in the central Andes using satellite data. J. Hydrometeor., 10, 167–182

804 [12] de Angelis CF, McGregor GR, Kidd C. 2004a. A 3 year climatology of rainfall characteristics over tropical
805 and subtropical SouthAmerica based on tropical rainfall measuring mission precipitation radar
806 data.International Journal of Climatology24: 385 – 399.
807 [13] JÖRG BENDIX,* RÜTGER ROLLENBECK and CHRISTOPH REUDENBACH, 2006. DIURNAL PATTERNS
808 OF RAINFALL IN A TROPICAL ANDEAN VALLEY OF SOUTHERN ECUADOR AS SEEN BY A
809 VERTICALLY POINTING K-BAND DOPPLER RADAR Int. J. Climatol. 26: 829–846 (2006)
810 [14] Weischet W. 1969. Climatological principles of the vertical distribution of rainfall in tropical mountains (in
811 German). Die Erde 100: 287–306.
812 [15] Rasmussen, K.L., Houze Jr, R.A., 2011. Orogenic convection in subtropical South America as seen by the
813 TRMM satellite. Mon. Wea. Rev., 139, 2399-2420.
814 [16] Romatschke, U., Houze Jr, R.A., 2010. Extreme summer convection in South America. J. Clim., 23, 3761-3791.
815 [17] Petersen, W.A. and Rutledge, S.A., 2001. Regional variability in tropical convection: Observations from
816 TRMM. *Journal of Climate*, *14*(17), pp.3566-3586.
817 [18] Qie, X. S., X. K. Wu, T. Yuan, J. C. Bian, and D. R. Lu (2014), Comprehensive pattern of deep convective
818 systems over the Tibetan Plateau-South Asian monsoon region based on TRMM data, J. Clim., 27, 6612–6626,
819 doi:10.1175/JCLI-D-14-00076.1.
820 [19] Xu, W., and E. J. Zipser (2012), Properties of deep convection in tropical continental, monsoon, and oceanic
821 rainfall regimes, Geophys. Res. Lett., 39, L07802, doi:10.1029/2012GL051242.
822 [20] Bhat, G. S., and S. Kumar, 2015: Vertical structure of cumulonimbus towers and intense convective clouds
823 over the South Asian region during the summer monsoon season. J. Geophys. Res. Atmos., 120, 1710–1722,
824 doi:10.1002/2014JD022552.
825 [21] Kumar, S., 2017a. A 10-year climatology of vertical properties of most active convective clouds over the
826 Indian regions using TRMM PR. Theoretical and applied climatology, 127(1-2), pp.429-440.
827 https://doi.org/10.1007/s00704-015-1641-5
828 [22] Liu, C. and Zipser, E.J., 2009. "Warm rain" in the tropics: Seasonal and regional distributions based on 9 yr
829 of TRMM data. *Journal of Climate*, *22*(3), pp.767-779.
830 [23] Kumar, S., Bhat, G. S., 2016. Vertical profiles of radar reflectivity factor in intense convective clouds in the
831 tropics. J. Appl. Meteoro. Climatol, 55(5), pp.1277-1286. https://doi.org/10.1175/JAMC-D-15-0110.1

[24] Kumar, S., 2017b. Vertical characteristics of reflectivity in intense convective clouds using TRMM PR data. Environment and Natural Resources Research, 7(2), p.58. https://doi.org/10.5539 /enrr.v7n2p58

[25] Kumar, S., 2018. Vertical structure of precipitating shallow echoes observed from TRMM during Indian summer monsoon. Theoretical and applied climatology, 133(3-4), pp.1051-1059. DOI 10.1007/s00704-017-2238-y

[26] Peters, G., Fischer, B., Münster, H., Clemens, M., Wagner, A., 2005. Profiles of raindrop size distributions as retrieved by microrain radars. J. Appl. Meteorol. 44, 1930–1949. http://dx.doi.org/10.1175/JAM2316.1.

[27] Thurai, M., Iguchi, T., Kozu, T., Eastment, J.D., Wilson, C.L., Ong, J.T., 2003. Radar observations in Singapore and their implications for the TRMM precipitation radar retrieval algorithms. Radio Sci. 38, 1086. http://dx.doi.org/10.1029/ 2002RS002855.

[28] Cluckie, I.D., Griffith, R.J., Lane, A., Tilford, K.A., 2000. Radar hydrometeorology using a vertically pointing radar. Hydrol. Earth Syst. Sci. 4, 565–580. http://dx.doi.org/ 10.5194/hess-4-565-2000.

[29] Schumacher, C. and Houze Jr, R.A., 2003. The TRMM precipitation radar's view of shallow, isolated rain. *Journal of Applied Meteorology*, *42*(10), pp.1519-1524.

[30] Zipser, E.J., Lutz, K.R., 1994. The vertical profile of radar reflectivity of convective cells: a strong indicator of storm intensity and lightning probability? Mon. Weather Rev. 122, 1751–1759.

[31] Kozu, T., Reddy, K.K., Mori, S., Thurai, M., Ong, J.T., Rao, D.N., Shimomai, T., 2006. Seasonal and diurnal variations of raindrop size distribution in Asian monsoon region. J. Meteorol. Soc. Jpn. 84A, 195–209.

[32] Rao, T.N., Radhakrishna, B., Nakamura, K., Rao, N.P., 2009. Differences in raindrop size distribution from southwest monsoon to northeast monsoon at Gadanki. Q. J. R. Meteorol. Soc. 135 (643), 1630–1637.

[33] Das, S., Maitra, A., Shukla, A.K., 2010a. Rain attenuation modeling in the 10–100 Ghz frequency using drop size distributions for different climatic zones in tropical India. Progr. Electromagn. Res. B 25, 211–224.

[34] Das, S., Shukla, A.K., Maitra, A., 2010b. Investigation of vertical profile of rain microstructure at Ahmedabad in Indian tropical region. Adv. Space Res. 45 (10), 1235–1243. http://dx.doi.org/10.1016/j.asr.2010.01.001.

[35] Kumar, S., Silva-Vidal, Y., Moya-Álvarez, A.S. and Martínez-Castro, D., 2019. Effect of the surface wind flow and topography on precipitating cloud systems over the Andes and associated Amazon basin: GPM observations. *Atmospheric Research*, *225*, pp.193-208.

[36] Das, S., Maitra, A., 2016. Vertical profile of rain: Ka band radar observations at tropical locations. Journal of Hydrology 534 (2016) 31–41

860 [37] Liu, C. and Zipser, E.J., 2013. Why does radar reflectivity tend to increase downward toward the ocean
861 surface, but decrease downward toward the land surface?. *Journal of Geophysical Research: Atmospheres*, *118*(1),
862 pp.135-148.
863 [38] Kirstetter, P.E., Gourley, J.J., Hong, Y., Zhang, J., Moazamigoodarzi, S., Langston, C. and Arthur, A., 2015.
864 Probabilistic precipitation rate estimates with ground-based radar networks. *Water Resources Research*, *51*(3),
865 pp.1422-1442.
866 [39] Sumesh, R.K., Resmi, E.A., Unnikrishnan, C.K., Jash, D., Sreekanth, T.S., Resmi, M.M., Rajeevan, K., Nita, S.
867 and Ramachandran, K.K., 2019. Microphysical aspects of tropical rainfall during Bright Band events at mid and
868 high-altitude regions over Southern Western Ghats, India. *Atmospheric Research*, *227*, pp.178-197.
869 [40] Rao, T.N., Rao, D.N., Mohan, K., Raghavan, S., 2001. Classification of tropical precipitating systems and
870 associated Z-R relationships. J. Geophys. Res. 106 (D16), 17699–17711. http://dx.doi.org/10.1029/2000JD900836.
871 [41] Das, S., Talukdar, S., Bhattacharya, A., Adhikari, A., and Maitra, A., 2011. Vertical profile of Z-R relationship
872 and its seasonal variation at a tropical location. In: Applied Electromagnetics Conference (AEMC), Kolkata, India,
873 Dec. 18–22, 2011. http://dx.doi.org/10.1109/AEMC.2011.6256915.
874 [42] Das, S., Maitra, A., Shukla, A.K., 2011b. Melting layer characteristics at different climatic conditions in the
875 Indian region: ground based measurements and satellite observations. Atmos. Res. 101 (1), 78–83.
876 [43] Schuur, T.J., Ryzhkov, A.V., Zrnić, D.S. and Schönhuber, M., 2001. Drop size distributions measured by a
877 2D video disdrometer: Comparison with dual-polarization radar data. *Journal of Applied Meteorology*, *40*(6),
878 pp.1019-1034.
879 [44] Francou, B., M. Vuille, P. Wagnon, J. Mendoza, and J.-E. Sicart. 2003. Tropical climate change recorded by a
880 glacier in the central Andes during the last decades of
881 [45] Perry, L. B., A. Seimon, and G. M. Kelly, 2014: Precipitation delivery in the tropical high Andes of southern
882 Peru: New findings and paleoclimatic implications. Int. J. Climatol., 34, 197–215,
883 [46] Endries, J.L., Perry, L.B., Yuter, S.E., Seimon, A., Andrade-Flores, M., Winkelmann, R., Quispe, N., Rado, M.,
884 Montoya, N., Velarde, F. and Arias, S., 2018. Radar-observed characteristics of precipitation in the tropical high
885 Andes of southern Peru and Bolivia. *Journal of Applied Meteorology and Climatology*, *57*(7), pp.1441-1458.
886 [47] Perry, L.B., Seimon, A., Andrade-Flores, M.F., Endries, J.L., Yuter, S.E., Velarde, F., Arias, S., Bonshoms, M.,
887 Burton, E.J., Winkelmann, I.R. and Cooper, C.M., 2017. Characteristics of precipitating storms in glacierized

888 tropical Andean cordilleras of Peru and Bolivia. *Annals of the American Association of Geographers*, *107*(2), pp.309-
889 322.
890 [48] Houze, R.A., 2012. Orographic effects on precipitating clouds. Rev. Geophys. 50. https://
891 doi.org/10.1029/2011RG000365.
892 [49] Battan, L.J., 1964. Some observations of vertical velocities and precipitation sizes in a thunderstorm. J. Appl.
893 Meteorol. 3, 415–420.
894 [50] Srivastava, R.C., 1971. Size distribution of raindrops generated by their breakup and coalescence. *Journal of*
895 *the Atmospheric Sciences*, *28*(3), pp.410-415.
896 [51] Low, T.B. and List, R., 1982. Collision, coalescence and breakup of raindrops. Part I: Experimentally
897 established coalescence efficiencies and fragment size distributions in breakup. *Journal of the Atmospheric Sciences*,
898 *39*(7), pp.1591-1606.
899 [52] Hu, Z. and Srivastava, R.C., 1995. Evolution of raindrop size distribution by coalescence, breakup, and
900 evaporation: Theory and observations. *Journal of the atmospheric sciences*, *52*(10), pp.1761-1783.
901 [53] Martins, R.C., Machado, L.A. and Costa, A.A., 2010. Characterization of the microphysics of precipitation
902 over Amazon region using radar and disdrometer data. *Atmospheric Research*, *96*(2-3), pp.388-394.
903 [54] Cha, J. W., S. S. Yum, K. H. Chang, and S. N. Oh, 2007: Estimation of the melting layer from a Micro Rain
904 Radar (MRR) data at the Cloud Physics Observa- tion System (CPOS) site at Daegwallyeong Weather Station. J.
905 Korean Meteor. Soc., 43, 77–85.
906 [55] Vuille, M. 1999. Atmospheric circulation over the Bolivian Altiplano during dry and wet periods and
907 extreme phases of the Southern Oscillation. International Journal of Climatology 19:1579–600.
908 [56] Oke, T. R., 1987: *Boundary Layer Climates.* 2d ed. Routledge, 435 pp
909 [57] Garreaud, R., Vuille, M. and Clement, A.C., 2003. The climate of the Altiplano: observed current conditions
910 and mechanisms of past changes. *Palaeogeography, palaeoclimatology, palaeoecology*, *194*(1-3), pp.5-22.
911 [58] Mohr, K. I., D. Slayback, and K. Yager, 2014: Characteristics of precipitation features and annual rainfall
912 during the TRMM era in the central Andes. J. Climate, 27, 3982–4001,
913 [59] Villalobos, E.E., Martinez-Castro, D., Kumar, S., Silva, Y. and Fashe, O., 2019. Estudio de tormentas
914 convectivas sobre los Andes Centrales del Perú usando los radares PR-TRMM y KuPR-GPM. *Revista Cubana de*
915 *Meteorología*, *25*(1), pp.59-75.

916 [60] Kumar, S., Silva, Y., Moya-Álvarez, A.S. and Martínez-Castro, D., 2019. Seasonal and Regional Differences
917 in Extreme Rainfall Events and Their Contribution to the World's Precipitation: GPM Observations. *Advances in*
918 *Meteorology*, *2019*.
919 [61] Sulca, J., Vuille, M., Silva, Y., Takahashi, K., 2016. Teleconnections between the Peruvian central Andes and
920 northeast Brazil during extreme rainfall events in austral summer. J. Hydrometeor., 17(2), pp.499-515
921 [62] Drumond, A., Nieto, R., Gimeno, L. and Ambrizzi, T., 2008. A Lagrangian identification of major sources of
922 moisture over Central Brazil and La Plata Basin. *Journal of Geophysical Research: Atmospheres*, *113*(D14).
923 [63] Garreaud, R. and Wallace, J.M., 1997. The diurnal march of convective cloudiness over the Americas.
924 *Monthly Weather Review*, *125*(12), pp.3157-3171.
925 [64] METEK, 2009: MRR physical basics: version 5.2.0.1. METEK Tech.Manual, 20
926 pp,http://www.mpimet.mpg.de/fileadmin/atmosphaere/barbados/Instrumentation/MRR-physical-
927 basics_20090707.pdf.
928 [65] Cha, J.W., Chang, K.H., Yum, S.S. and Choi, Y.J., 2009. Comparison of the bright band characteristics
929 measured by Micro Rain Radar (MRR) at a mountain and a coastal site in South Korea. *Advances in Atmospheric*
930 *Sciences*, *26*(2), pp.211-221.
931 [66] White, A. B., and D. J. Gottas, E. T. Strem, F. M. Ralph, and P. J. Neiman, 2002: An automated bright band
932 height detection algorithm for use with Doppler radar spectral moment. J. Atmos. Oceanic Technol., 19, 687–697.
933 [67] Tokay, A., Hartmann, P., Battaglia, A., Gage, K.S., Clark, W.L., Williams, C.R., 2009. A field study of
934 reflectivity and Z-R relations using vertically pointing radars and disdrometers. J. Atmos. Oceanic Technol. 26,
935 1120–1134. http://dx.doi.org/ 10.1175/2008JTECHA1163.1.
936 [68] Fabry, F., Zawadzki, I., 1995. Long-term radar observations of the melting layer of precipitation and their
937 interpretation. J. Atmos. Sci. 52, 838–851
938 [69] Barthazy, E., Henrich, W., Waldvogel, A., 1998. Size distribution of hydrometeors through the melting layer.
939 Atmos. Res. 47–48, 193–208. https://doi.org/10.1016/ S0169-8095(98)00065-9.
940 [70] Heymsfield, G.M., Tian, L., Heymsfield, A.J., Li, L. and Guimond, S., 2010. Characteristics of deep tropical
941 and subtropical convection from nadir-viewing high-altitude airborne Doppler radar. *Journal of the Atmospheric*
942 *Sciences*, *67*(2), pp.285-308.
943 [71] Williams, C.R., Ecklund, W.L., Gage, K.S., 1995. Classification of precipitating clouds in the tropics using
944 915 MHz wind profilers. J. Atmos. Ocean. Technol. 12, 996–1012.

945 [72] Glickman, T. S., 2000: Glossary of Meteorology. 2d Ed. Amer. Meteor. Soc., 855pp.

946 [73] Zawadzki, I., W. Szyrmer, C. Bell, and F. Fabry, 2005: Modeling of the melting layer. Part III: The density
947 effect. J. Atmos. Sci., 62, 3705–3723.

948 [74] Thurai, M., Gatlin, P.N., Bringi, V.N., 2016. Separating stratiform and convective rain types based on the
949 drop size distribution characteristics using 2D video disdrometer data. Atmos. Res. 169 B, 416–423.
950 https://doi.org/10.1016/j.atmosres.2015.04.011.

951 [75] Kumar, S. and Silva, Y., 2019. Vertical characteristics of radar reflectivity and DSD parameters in intense
952 convective clouds over South East South Asia during the Indian Summer monsoon: GPM observations.
953 *International Journal of Remote Sensing*, pp.1-25.

954 [76] Prat, O.P., Barros, A.P., 2010. Ground observations to characterize the spatial gradients and vertical structure
955 of orographic precipitation – experiments in the inner region of the Great Smoky Mountains. J. Hydrol. 391 (1–
956 2), 141–156.

957 [77] Gatlin, P., Petersen, W., Knupp, K. and Carey, L., 2018. Observed Response of the Raindrop Size Distribution
958 to Changes in the Melting Layer. *Atmosphere*, *9*(8), p.319.

959 [78] Pruppacher, H.R. and Klett, J.D., 2010. Microstructure of atmospheric clouds and precipitation. In
960 *Microphysics of Clouds and Precipitation* (pp. 10-73). Springer, Dordrecht.

961 [79] Austin, P. M., and A. C. Bernis, 1950: A quantitative study of the ''bright band'' in radar precipitation echoes.
962 J. Meteor., 7, 145–151

963 [80] Simões Reboita, M.; Krusche, N.; Ambrizzi, T.; Porfírio da Rocha, R. Entendendo o Tempo e o Clima na
964 América do Sul. Terra Didatica **2012**, 8, 34–50.

965 [81]Garstang, M., Massie Jr, H.L., Halverson, J., Greco, S. and Scala, J., 1994. Amazon coastal squall lines. Part I:
966 Structure and kinematics. *Monthly Weather Review*, *122*(4), pp.608-622.

967 [82] Lasher-Trapp, S., Kumar, S., Moser, D.H., Blyth, A.M., French, J.R., Jackson, R.C., Leon, D.C. and Plummer,
968 D.M., 2018. On different microphysical pathways to convective rainfall. *Journal of Applied Meteorology and*
969 *Climatology*, *57*(10), pp.2399-2417.

970 [83] Garreaud, R. D. 1999. Multiscale analysis of the summer-time precipitation over the central Andes. Monthly
971 Weather Review 127:901–21.

972 [84] Houze, R. A., 1997. Stratiform precipitation in regions of convection: A meteorological paradox? Bulletin of
973 the American Meteorological Society 78:2179–96.

974 [85] Yuter, S. E., D. Kingsmill, L. B. Nance, and M. L€ offler-Mang. 2006. Observations of precipitation size and
975 fall speed characteristics within coexisting rain and wet snow. Journal of Applied Meteorology and Climatology
976 45:1450–64.
977 [86] Chavez, S. P., and K. Takahashi, 2017: Orographic rainfall hot spots in the Andes-Amazon transition
978 according to the TRMM precipitation radar and in situ data. J. Geophys. Res. Atmos., 122, 5870–5882,
979 https://doi.org/10.1002/2016JD026282.
980 [87] Rabatel, A., Francou, B., Soruco, A., Gomez, J., Cáceres, B., Ceballos, J.L., Basantes, R., Vuille, M., Sicart, J.E.,
981 Huggel, C. and Scheel, M., 2013. Current state of glaciers in the tropical Andes: a multi-century perspective on
982 glacier evolution and climate change.
983 [88] Salzmann, N., C. Huggel, M. Rohrer, W. Silverio, B. G. Mark, P. Burns, and C. Portocarrero. 2013. Glacier
984 changes and climate trends derived from multiple sources in the data scarce Cordillera Vilcanota region,
985 Southern Peruvian Andes. The Cryosphere 7:103–18.
986 [89] Houze, R. A., Jr. 1993. Cloud dynamics. San Diego, CA: Academic.